AGU PUBLICATIONS

JGR

Journal of Geophysical Research: Solid Earth

RESEARCH ARTICLE

10.1002/2016JB013803

Key Points:
- Massive limestones deform seismically; aseismic creep is observed only in volcanic rocks with clay gouges
- Clay gouges result from transformations of rocks during seismic and aseismic deformation
- Aseismic creep mechanism is a combination of pressure solution viscous creep and grain frictional sliding

Supporting Information:
- Supporting Information S1

Correspondence to:
F. Renard,
francois.renard@geo.uio.no

Citation:
Kaduri, M., J.-P. Gratier, F. Renard, Z. Çakir, and C. Lasserre (2017), The implications of fault zone transformation on aseismic creep: Example of the North Anatolian Fault, Turkey, *J. Geophys. Res. Solid Earth*, *122*, doi:10.1002/2016JB013803.

Received 29 NOV 2016
Accepted 8 MAY 2017
Accepted article online 10 MAY 2017

©2017. American Geophysical Union. All Rights Reserved.

The implications of fault zone transformation on aseismic creep: Example of the North Anatolian Fault, Turkey

Maor Kaduri[1], Jean-Pierre Gratier[1], François Renard[1,2], Ziyadin Çakir[3], and Cécile Lasserre[1]

[1]ISTerre, University Grenoble Alpes and CNRS, Grenoble, France, [2]Department of Geosciences, Physics of Geological Processes, University of Oslo, Oslo, Norway, [3]Department of Geology, Istanbul Technical University, Istanbul, Turkey

Abstract Aseismic creep is observed at surface along several segments of the North Anatolian right-lateral active fault in Turkey, a major plate boundary between Eurasia and Anatolia. Identifying the mechanisms that control creep and their temporal and spatial change represents a major challenge for predicting the mechanical evolution of active faults, the interplay between creep and earthquakes, and the link between short-term observations from geodesy and the long-term fault zone evolution. We combine geological observations, laboratory analyses, and imaging techniques, shedding new light on the mechanism of fault creep along the North Anatolian Fault (NAF) and its time-dependent change. A clear correlation is shown between shallow creep and near-surface fault gouge composition: locked segments of the NAF are mostly composed of massive limestones without clay gouges, whereas creeping segments comprise clay gouges that contain low-friction minerals. Such fault gouges appear to result from a progressive change of initial volcanic host rocks during their deformation. Anastomosing cleavage develops during the first stage of displacement, leading to layering, oblique at first and then subparallel to the fault, which accommodates part of the aseismic creep by pressure solution. Soluble minerals are dissolved, leading to passive concentration of phyllosilicates in the gouges where alteration transformations by fluid flow produce low friction minerals. At the same time damage zones are fractured and fractures are sealed by carbonates. As a result, these mineralogical and structural transformations weaken the gouge and strengthen the damage zone leading to the change from diffuse to localized seismic-aseismic zones.

1. Introduction

Active shallow aseismic displacement, also called creep, has been measured on several major continental faults such as the San Andreas Fault in California [*Titus et al*., 2006; *de Michele et al*., 2011], the Haiyuan Fault in China [*Jolivet et al*., 2012, 2013, 2015], the El-Pilar Fault in Venezuela [*Jouanne et al*., 2011; *Pousse Beltram et al*., 2016], the Longitudinal Valley Fault in Taiwan [*Thomas et al*., 2014b], the Chaman Fault in Pakistan [*Fattahi and Amelung*, 2016], and the North Anatolian Fault in Turkey along the Ismetpasa segment [*Ambraseys*, 1970*; Barka*, 1992*; Çakir et al*., 2005*; Kaneko et al*., 2013*; Cetin et al*., 2014]. Creep behavior can be permanent, or it can appear after a major earthquake and be called afterslip or postseismic creep, as measured, for example, from slow surface displacements over a period of several years following the 1999 Izmit earthquake in Turkey [*Çakir et al*., 2003; *Hearn et al*., 2009, *Hussain et al*., 2016a].

Creep, in addition to silent slow slip events, tremors, and repeating earthquakes, sheds new light on the dynamics of the Earth's continental crust at a global scale and on the seismic cycle [*Peng and Gomberg*, 2010*; Beroza and Ide*, 2011*; Barbot et al*., 2012]. The existence of physical and geological links between all these phenomena is strongly suggested by observations of foreshocks and repeating earthquakes prior to some large earthquakes [*Bouchon et al*., 2011, 2013]. These observations are interpreted as resulting from the nucleation phase, involving creep on or around the future rupture area. Because small or slow earthquakes and creep processes transfer stress between different portions of the fault, relaxing or loading them [*Stein et al*., 1997], they could trigger the nucleation of large earthquakes.

The North Anatolian Fault (NAF) is a continental right-lateral fault that separates the Anatolian Plate to the south and the Eurasian Plate to the north (Figure 1). Its main active trace has a sharp morphological expression. Large-scale structural right-lateral offsets have been estimated, as that of the Pontide suture [*Şengör et al*., 1985; *Hubert-Ferrari*, 2002] or around the Sea of Marmara [*Barka*, 1992*; Le Pichon*, 2003*; Armijo et al*., 2005*; Şengör et al*., 2005; *Akbayram et al*., 2016] and in the western part of the central bend [*Hubert-Ferrari*, 2002]. In western Turkey, slip between Anatolia and Eurasia is partitioned on several fault branches

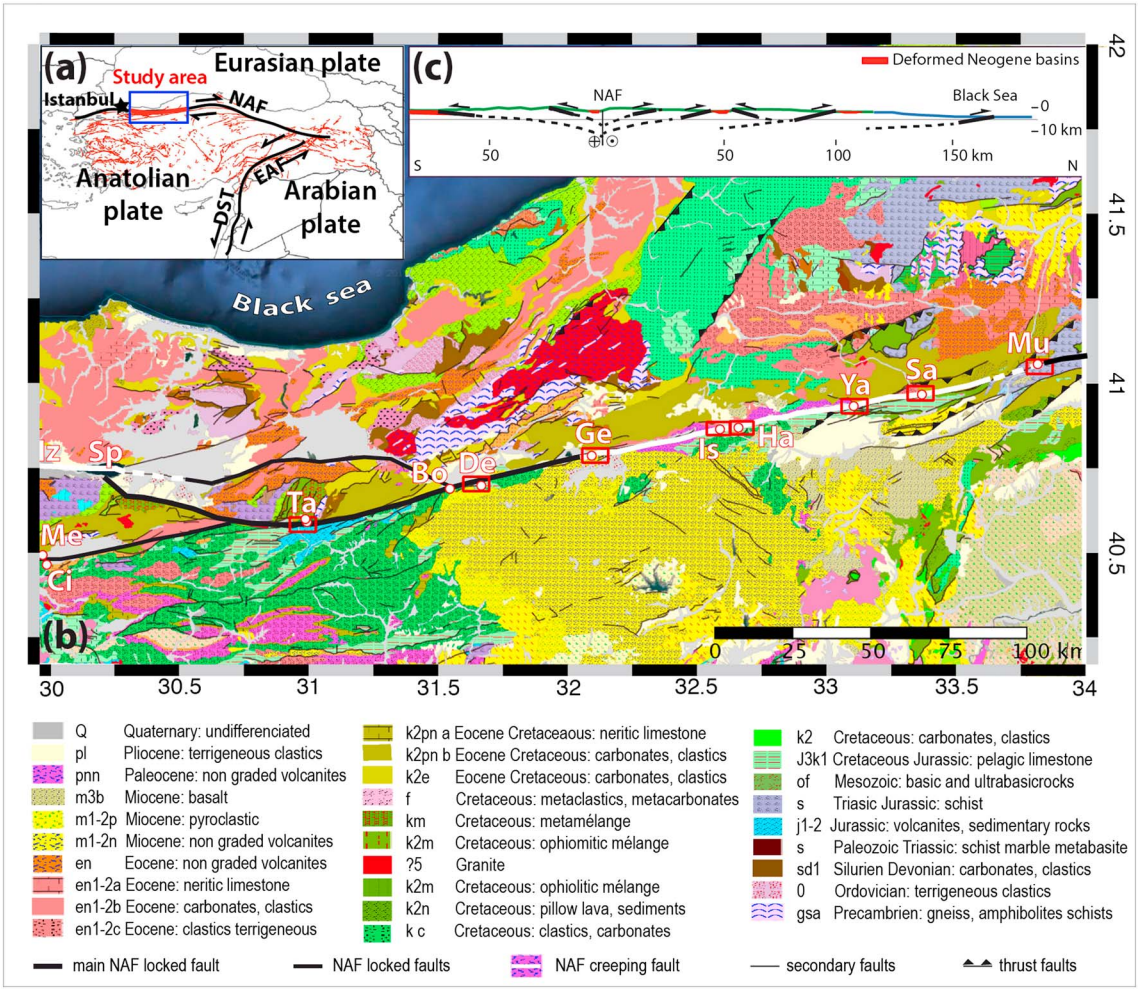

Figure 1. Structural and geological map of the study area along the North Anatolian Fault: (a) Location map of Turkey. The study area, east of Istanbul, is marked by a blue rectangle with the studied fault segment in red [*Emre et al.*, 2013]. NAF: North Anatolian Fault, EAF: East Anatolian Fault, and DST: Dead-Sea Transform fault segment. (b) Geological map of the study area with names and outcrop locations indicated as white circles: Me = Mekece, Ci = Ciciler, Iz = Izmit, Sp = Sapanca lake, Ta = Taskesti, Bo = Bolu, De = Demirciler, Ge = Gerede, Is = Ismetpasa, Ha = Hamamli, Ya = Yazioren, Sa = Sarialan, and Mu = Mülayim. The creeping segments of Izmit (west) and Ismetpasa (east) are marked in white [*Çakir et al.*, 2005; *Cetin et al.*, 2014]. The locked segments are black. Small red rectangles contour local geological maps shown in the following figures to describe outcrops with referenced names. The GPS coordinates of these outcrops are given in the supporting information. The regional geological map is extracted from an interactive map of the Turkish geological survey [*Akbaş et al.*, 2016] available on http://yerbilimleri.mta.gov.tr/anasayfa.aspx. The legend gives the lithology of the formations that are cut by the studied NAF segment. (c) Schematic N-S cross section along the eastern boundary of the map, adapted from [*Yildirim et al.*, 2011].

[*Ambraseys*, 1970; *Hubert-Ferrari*, 2002; *Flerit et al.*, 2003]. Together, they amount to about 80 km total displacement [*Armijo et al.*, 1999, 2000]. This cumulative displacement along the North Anatolian Fault is in agreement with the analysis of major river deflections [*Barka*, 1992; *Hubert-Ferrari*, 2002; *Şengör et al.*, 2005]. Furthermore, measuring and dating stream channel and alluvial terraces offsets lead to Quaternary slip rate estimates of 18 mm/yr to 20.5 mm/yr [*Hubert-Ferrari*, 2002; *Kozaci et al.*, 2007, 2009; *Gasperini et al.*, 2011; *Meghraoui et al.*, 2012; *Grall et al.*, 2013], which can be compared to the present-day slip rate estimated from rigid block modeling of GPS measurements of about 17 to 27 mm/yr [*Barka and Reilinger*, 1997; *Straub et al.*, 1997; *McClusky et al.*, 2000; *Meade et al.*, 2002; *Reilinger et al.*, 2006, 2010]. Whether the variability in the fault slip rate estimates may be explained by slip partitioning between the different fault branches is still debated. With a mean slip rate of 20 mm/yr the displacement could have taken about 4 Ma to accumulate 80 km of displacement.

A striking feature of the North Anatolian Fault is the existence of different segments that show differing slip behaviors indicative of differing mechanical behaviors. Some segments remain locked and are prone to major earthquakes [*Ambraseys*, 1970; *Stein et al.*, 1997], while others display active aseismic or postseismic

creep measured using radar interferometry in particular [*Kaneko et al*., 2013*; Cetin et al*., 2014*; Hussain et al*., 2016a; *Rousset et al*., 2016]. According to *Kondo et al*. [2010], the Bolu-Gerede locked segment shows a recurrence time of earthquakes of about 330 years. Two inland segments of the North Anatolian Fault show aseismic creep [*Ambraseys*, 1970*; Çakir et al*., 2005, 2012*; Kaneko et al*., 2013*; Cetin et al*., 2014; *Hussain et al*., 2016b] (Figure 1). The 50 km long Izmit segment has been creeping since the 1999 earthquake [*Çakir et al*., 2012]. The fault segment near Ismetpasa has been creeping since at least the 1950s, possibly since the 1944 (M_w 7.2) and/or 1951 (M_w 6.9) earthquakes [*Çakir et al*., 2005] (Figure 1). Interferometric synthetic aperture radar (InSAR) studies determined the length of the Ismetpasa creeping segment as ~100 km, with a creep depth of ~7 km and an ~8 mm/yr creep rate [*Çakir et al*., 2005*; Kaneko et al*., 2013*; Cetin et al*., 2014; *Hussain et al*., 2016b]. This rate has been decreasing since the initial observations (1957–1969), in favor of a postseismic creep interpretation. The surface creep rate today is in overall less than half of the annual average rate of relative plate velocity, indicating that significant stress is still being accumulated on the fault [*Hussain et al*., 2016b]. Recent creepmeter and time-lapse InSAR studies also showed that creep occurs as bursts, with a depth up to 6 ± 3 km [*Rousset et al*., 2016; *Bilham et al*., 2016].

InSAR studies show that there is little differential vertical motion along the NAF in the Ismetpasa region [*Hussain et al*., 2016b]. However, thrust faults subparallel to the NAF that deform Neogene deposits are seen on the geological map and the cross section attesting of regional uplift (Figure 1). Geomorphological field observations of uplifted marine deposits also show that the NAF surface and fault rocks are uplifted versus the abyssal plain of the Black Sea with associated erosional processes. This late Neogene and active orogenic uplift is associated with the NAF displacement [*Yildirim et al*., 2011]. This means that outcropping rocks in the fault zone may gather samples deformed at various depths, from the surface to several kilometers deep.

From these field observations, the detailed mechanisms of creep at the scale of the fault zone remain to be understood. At least three deformation processes have been identified to explain a creep rheology of the rocks at low temperature and moderate stress in the upper crust: (1) pressure solution stress-driven viscous creep [*Elliott*, 1973*; Rutter*, 1976*; Gratier et al*., 2011, 2013b], (2) brittle creep [*Atkinson*, 1984*; Perfettini and Avouac*, 2004*; Brantut et al*., 2013], and (3) velocity-strengthening grain frictional sliding [*Marone*, 1998] where weak minerals are involved [*Moore and Rymer*, 2007*; Carpenter et al*., 2011a*; Lockner et al*., 2011]. Mixed friction and viscous creep behavior has also been proposed [*Bos and Spiers*, 2002]. These mechanisms depend to a variable degree on thermodynamic parameters (pressure and temperature), rock microstructure (size and shape of the grains), and mineral composition. Which of these three mechanisms is dominant in creeping fault zones is an open question.

The aims of this study are to characterize fault zone outcrops along creeping versus locked segments along the North Anatolian Fault and to identify the deformation mechanisms at the origin of creep. For this purpose, a detailed microstructural and mineralogical study of fault outcrops along the North Anatolian Fault is performed in order to answer the following questions: (1) Do the creeping segments correspond to specific geological and structural features along the fault? (2) What are the mechanisms of creep (friction versus stress-driven mass transfer), and how are the nature of rocks and fluids and the conditions of the deformation linked to these mechanisms? And (3) more generally, are the fault zone petrophysical properties different along the creeping zones versus the locked ones, and do these properties change with time?

2. Approach and Methodology

2.1. Fault Zone Outcrops

The present work studies the fault rock development and character of the North Anatolian Fault between Ciciler and Sapanca in the west to Mülayim in the east (Figure 1). This portion of the fault covers several segments, including the creeping segment of Ismetpasa [*Çakir et al*., 2005], from Gerede to Mülayim, and the locked segments from Sapanca and Ciciler to Gerede (Figure 1). To analyze the anatomy of the fault zones at the outcrop scale along these segments, field studies were performed that systematically followed the fault zone over a distance of 270 km. All outcrops that were located on the fault within 1 km of any tarred or accessible dirt road were explored. For this purpose, satellite images and the map of the faults provided by the Turkish geological survey [*Herece and Akay*, 2003] were used and dirt roads identified using Google Earth. More than 30 sites along both locked and creeping segments of the fault were visited where geomorphological evidence of the active fault can be identified (fresh outcrops, push-ups, offsets of streams, offsets

of lines of trees or walls, and sets of aligned springs or ponds). Seventeen well-preserved outcrops have been selected from these sites based on two criteria: (1) the fault zone is not fully covered by Quaternary sediments and (2) an outcropping cross section of the fault zone can be identified, with visible damage zone and core of the fault and in several cases the initial host rock as well. A dozen of the most representative outcrops are presented here (Figure 1b). Their GPS coordinates are given in the supporting information. From these outcrops, 90 oriented hand samples were collected and analyzed in the laboratory and 130 thin sections of rock samples were prepared for mineralogical, geochemical, and microstructural analyses. Several samples were collected from initial rock, damaged rock, and fault gouge: each type of rock was sampled in several places in order to determine the spatial variation of the mineralogy within the fault zone.

2.2. Sampling Procedure

In places where the samples were sufficiently cohesive, they were first oriented on the outcrop, localized with respect to their distance from the fault core, and then sampled with a hammer. In other places along the creeping segment, the rocks in the fault zone were very fragile due to both high damaging and high content of weak minerals. As a result, these rocks had a very low cohesion and sampling was challenging. We decided to sample them directly in the field using hollow metal tubes (5 cm internal diameter) that could be hammered directly into the gouge. The 20 cm long core samples were extracted. These samples were then immediately placed in a plastic bag that was sealed to avoid water evaporation. In this way, the internal structure of the gouge can be preserved. All tubes were oriented on the outcrop and labeled accordingly. Samples of damage zones and initial rocks, located up to a hundred meters from the fault core, were also collected. In order to prepare oriented thin sections, the samples should be cut without compromising the microstructures. The less cohesive samples were consolidated using PRESI epoxy resin diluted with 10% methanol in vacuum. These samples in their epoxy bath were placed in a vacuum glass chamber for 1 day. Using this procedure, the epoxy can access large and small pores and consolidate the sample sufficiently for thin section preparation without compromising chemical and structural analyses.

2.3. Chemical, Mineralogical, and Microstructural Analyses of Fault Samples

The mineralogy, chemistry, and microstructures were characterized and quantified using a series of complementary analytical methods. The chemical compositions were obtained at various scales leading to maps of oxide contents at various sizes: X-ray fluorescence imaging (XRF) at sizes of several millimeters to centimeters, scanning electron microscopy (SEM-EDS) at sizes of several millimeters, and electron microprobe (EPMA) at sizes of several hundreds of microns with single points of local analysis (microns sizes). The mineralogical composition can be calculated if the minerals present in the sample are known. Such information was obtained from powder X-ray diffraction analyses that have been done at hand sample sizes (millimeters to centimeters and minerals were quantified using Rietvel refinement procedure [*Doebelin and Kleeberg*, 2015]). Mineral composition was then obtained either from internal programs (EPMA) or by the use of the XmapTool software [*Lanari et al*., 2014] for the other analyses. The microstructures were obtained from optical and SEM imaging. Details on analytical techniques are given in the supporting information.

When comparing composition contents between initial and deformed rocks, a distinction was made between soluble and insoluble minerals by reference to the abundant bibliography (see a review in *Gratier et al*. [2013a]). The most soluble minerals such as quartz, feldspars, calcite, and dolomite are considered to be mobile and are transported in solution during the deformation processes either by diffusion or by advection. Some of these minerals (quartz and carbonates) fill fractures. The most insoluble minerals such as phyllosilicates, Ti and Fe oxides, are considered to be nonmobile and are passively concentrated into the deformed rock. In order to best visualize the mass transfer processes, heterogeneously deformed zones are divided into homogeneous areas that are then sorted according to their soluble and insoluble mineral contents, respectively *Gratier et al*. [2013a]. This can be done at all scales from the outcrop to the grain size.

3. Results

3.1. Characteristics of the Locked Segments

Along the presently locked studied segments, all the fault outcrops we found in small or big quarries, from Sapanca Lake to Gerede, crosscut limestone lithology (Figure 1b). The total right-lateral fault offset of reference geological formations, along the Bolu-to-Mülayim NAF fault segment, is about 80 km. East of Bolu the

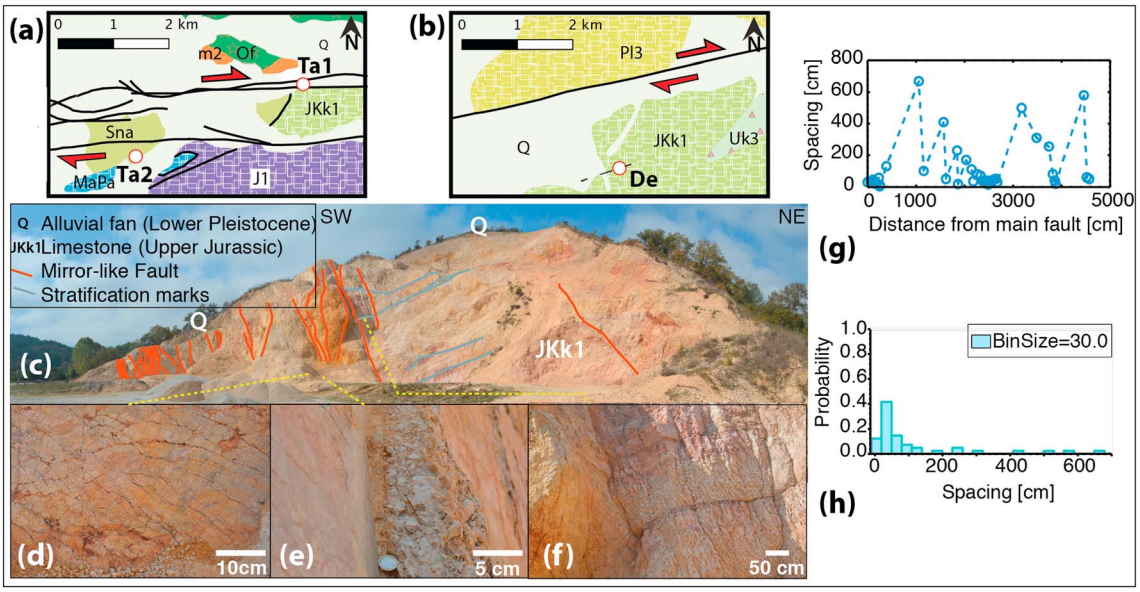

Figure 2. Taskesti and Dermirciler outcrops location and Taşkesti-1 fault structure; (a and b) Taskesti and Demirciler geological maps respectively; see lithology in Figure 7e. (c) The Taskesti-1 fault zone is located in an abandoned quarry, and numerous localized slip surfaces can be seen. (d) Mirror-like slip surface. (e) Limestone gouge. (f) Damage zone (mainly by fracturing). (g) Spacing between the slip surfaces as a function of the distance from the main fault. (h) Probability density function of the distances between slip surfaces with the most frequent distance close to 45 cm (see the supporting information for detailed method).

NAF splits into several branches with various offsets: 50 km along the Taskesti-Sapanca main segment and 30 km along the Taskesti-Ciciler and North-Taskesti segments [*Akbayram et al.*, 2016]. The Sapanca-to-Gerede fault segment puts in contact mostly carbonates-clastics and limestone massifs. Its northern compartment comprises carbonates-clastics and limestone massif, more than 5 km thick [*Göncüoglu*, 2010], that are seen along about 90% of the total 200 km long fault segment only locally interrupted by NE-SW trending stripes of Paleozoic schist and marble as well as Eocene volcanic rocks extending over distance of about 10% of the total along-the-fault length. The southern compartment of this Sapanca-to-Gerede fault segment comprises a huge massif of Eocene to Jurassic carbonates-clastics and limestones, also several kilometers thick, extending along about 90% of the 200 km long fault segment only locally interrupted by some NE-SW trending stripes of volcanic rocks extending over distance of about 10% of the along-the-fault length. The same 90% carbonates-clastics and limestones versus 10% volcanic rocks ratio is seen along the Taskesti-Ciciler branch (comprising the Mekece and Ciciler outcrops) Figure 1. In terms of deformation style the locked fault segment shows localized deformation structures such as cataclastic bands, mirror-like slip surfaces, gouges of various width, horizontal striaes, tectonic stylolites, and anastomosing slip surfaces.

3.1.1. Taşkesti Outcrop

The main outcrop (Ta1, Figure 2a) is located east of the Taşkesti settlement (Figure 1) in an abandoned quarry in massive limestone (JKk1). The fault zone is oriented parallel to the main trend of the North Anatolian Fault. It is made up of a succession of several subparallel main slip surfaces, with near-horizontal striaes, embedded in damage zones (Figure 2c). The outcrop is located along the 1967 earthquake rupture, and some of the slip surfaces may be related to this event. Of the ~200 m wide damage zone, only an ~50 m wide section is freshly outcropping, with arrays of subparallel near-vertical fault surfaces and 4–6 m wide near-vertical cataclastic deformation zones crosscutting the limestone (Figure 2c). Figure 2d shows examples of mirror fault surfaces with fracture networks. Most of the faults are associated with gouges made of fine-grained calcite powder with widths measured in millimeters to centimeters (Figure 2e). Their clay contents are always very low (less than 5%) and not very different from the host rocks (less than 2%). In thin sections, mirror faults show much higher contents in Fe oxides than in the host rocks. The spacing of the slip surfaces plotted as a function of distance from the main fault shows two zones with a high density of slip surfaces (Figure 2g). The probability density function of the discretized fracture spacing (bin size = 30 cm) shows lognormal distribution, and the most frequent spacing distance is 45 cm (Figure 2h). Two main types of deformation microstructures are

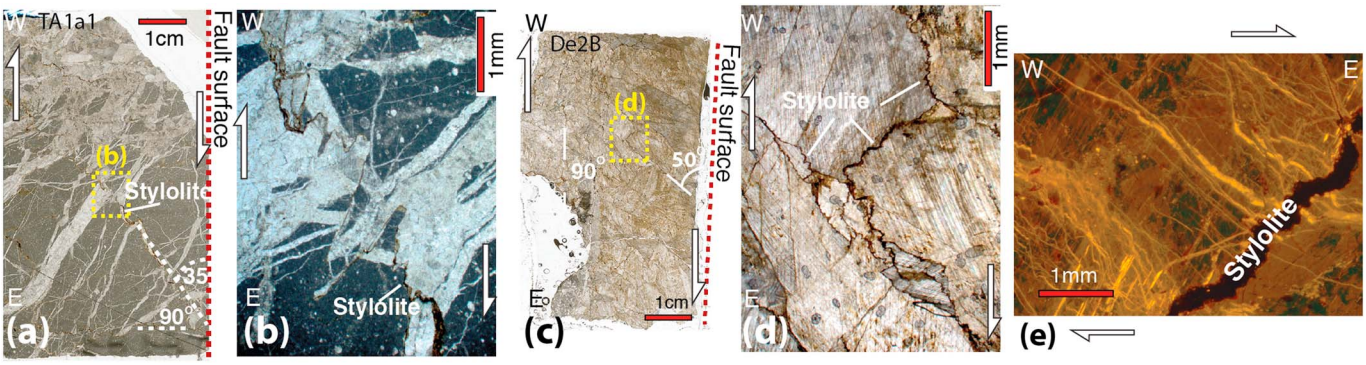

Figure 3. Microstructures of the deformed zones. Taşkesti-1 outcrop: (a) Horizontal thin section in limestone (arrows are parallel to the strike-slip fault) with networks of vertical tectonic stylolites and veins. Stylolite surfaces are seen here crosscutting at 35° and 90° with respect to the fault plane although these surfaces may be inclined at any angle to the fault plane. The stylolite peaks indicate an orientation of the main horizontal compressive stress that varies from near parallel to near perpendicular to the fault. (b) Magnified view of the yellow rectangle in Figure 3a where a stylolite crosscuts a preexisting vein, underlying the shortening direction due to pressure solution. Demirciler outcrop: (c) Horizontal thin section showing vertical tectonic stylolites crosscutting in all directions with respect to the strike slip fault. (d) Magnified view of the yellow rectangle in Figure 3c showing calcite twinning in the microlithons. (e) In horizontal thin section, cathodoluminescence image of a vertical stylolite with perpendicular vertical tension gashes calcite veins probably indicating a closed system where the calcite dissolved in stylolites and sealed the nearby fractures.

observed in the limestone: cataclastic zones and tectonic stylolites. The cataclastic zones are composed mainly of angular fragments of limestone and calcite veins (Figure 2f). Within the vertical fault zones, vertical tectonic stylolites surfaces appear at any angle between 0 and 90° with respect to the fault plane (Figure 3a). The stylolite peaks indicate a horizontal main compressive stress ranging from near parallel to near perpendicular to the fault. The damage zones show near-vertical veins at any angle between 0 and 90° with respect to the fault plane. In places, those veins are crosscut and dissolved by stylolites that indicate the shortening axis (Figure 3b). Another outcrop nearby (Ta2, Figures 1 and 2a), located in massive Cretaceous limestone, shows the same type of structures.

3.1.2. Demirciler Outcrop

This outcrop (De, Figure 1) is an active quarry that exposes an ~100 m wide shear zone hosted in Jurassic limestone (JKk1, Figure 2b). The damage zone contains a dozen main slip surfaces with associated cataclastic zones, similar to the Taşkesti outcrops. Here the fault also contains networks of near-vertical tectonic stylolites oriented in the same directions versus the near-vertical faults as in Taskesti. They are also associated with vertical tension gashes veins (Figure 3e). Microlithons show calcite twinning (Figures 3c and 3d).

3.1.3. Common Characteristics

In summary, three main observations can be made regarding the Taskesti and Dermirciler outcrop sites (Ta and De, Figures 2 and 3) that are common to other ones (Ciciler, Mekece, and Bolu) along locked fault segments (Ci, Me, and Bo, Figure 1).

1. Displacement along the fault is associated with two different types of structures: (i) mirror-like fault surfaces with relatively high Fe oxides concentration together with very narrow cataclastic gouges and nearby vein fracture arrays with damage followed by healing and (ii) shear zones of centimeter to decimeter thickness and oriented parallel to the mirror faults contain numerous tectonic stylolites that are indicative of pressure solution creep processes [*Janssen et al.*, 1997].
2. Comparative chemical analyses of the damage zones and the shear zones versus the initial rocks show almost no change in the overall chemical composition. Local chemical differentiation may be seen in the stylolites that passively concentrate the insoluble species and in veins that are filled with pure calcite. Because vertical stylolites surfaces and tension gashes veins are clearly associated with right-lateral movement, this postseismic aseismic deformation must occur with a mean mass transfer distance from dissolution to reprecipitation zones of about 1 to 10 cm.
3. In several places, near-vertical vein arrays and tectonic stylolite surfaces occur at various angles with respect to the near-vertical fault surfaces: stylolite peaks (parallel to the local maximum compressive stress) and veins (perpendicular to the local minimum compressive stress) range from parallel to perpendicular to the strike-slip faults, indicating a rotation of the stress components with time (Figures 2 and 3).

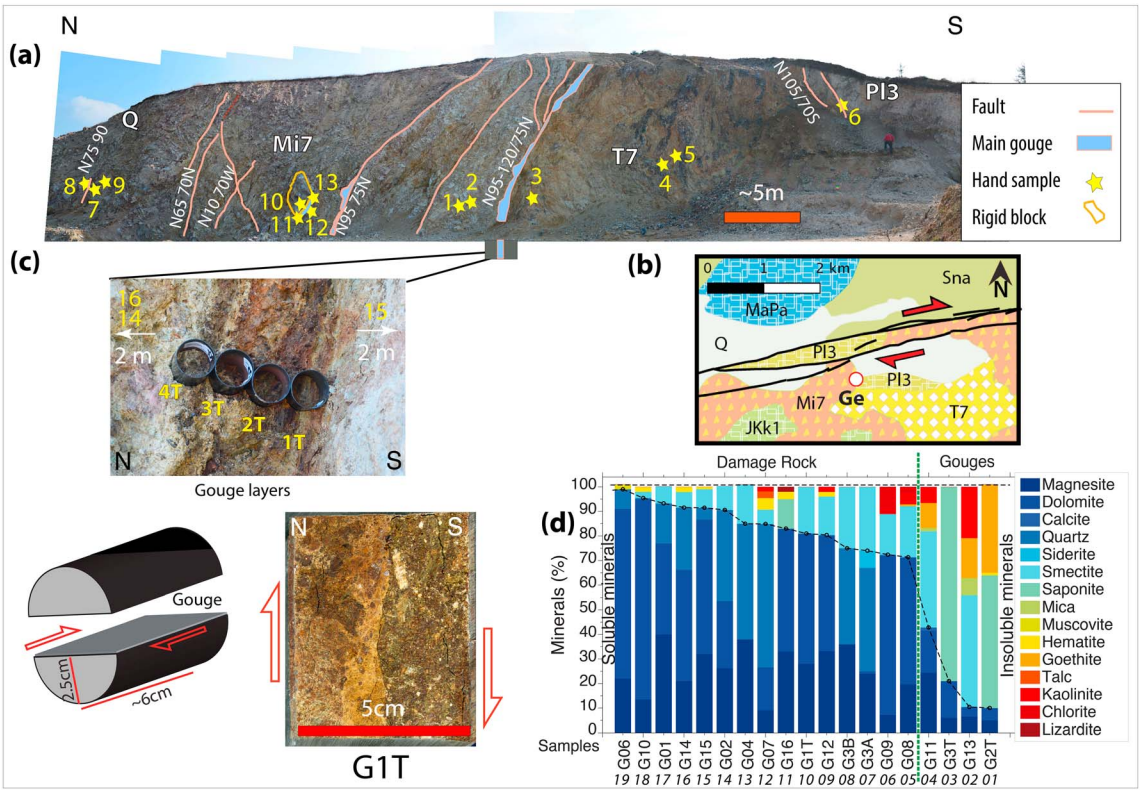

Figure 4. Gerede outcrop: general observation; see lithology in Figure 7e. (a) Photograph of the fault zone with the main structures and location of the sampling sites (yellow stars with G numbers). (b) Geological map. (c) Fault with gouge layers (with various white, red, or green colors). Each layer having different mineral contents was sampled using metal tubes labeled 1T to 4T. The sketch shows how the gouge was sampled, consolidated, and then cut to prepare thin sections with an example of horizontal slice of gouge sample after consolidation. Red arrows indicate the direction of horizontal slip on the main surface. (d) XRD analyses of mineral contents. The sample numbers are those shown on the outcrops of Figure 4c; see supporting information for detailed content. The samples have been sorted according to their content in soluble and insoluble minerals. The green dashed line separates damaged rock samples from those of the gouge that contain much more insoluble minerals than the damage zones. The G1T sample of gouge is rich in parallel-to-the-gouge altered carbonate veins. Sample G10 is a piece of a rigid block that is mainly composed of carbonate veins in contact with a clay gouge (samples G11–G13).

3.2. Characteristics of the Ismetpasa Creeping Segment

Unlike the locked segments, the Ismetpasa creeping segment exhibits several rock lithologies, with wide variations in mineral composition, microstructure, and fault structure but without any outcrops of limestone. At regional scale, there is a major geological transition between the locked segment (from Sapanca to Gerede) and the creeping segment (from Gerede to Mülayim). The creeping segment crosses the northern part of the huge Miocene to Paleocene Volcanic Galatia massif that extends about 200 km east-west and 200 km north-south, Figure 1b [*Akbaş et al.*, 2016]. In more details, the creeping fault segment lies for 90% of its length within the volcanic units and cuts narrow stripes of limestone and clastic rocks on less than 10% of its length. The total fault offset, of about 80 km, puts face to face the volcanic units either with other volcanic units or with sandstones, serpentines, or a near-continuous stripe of limestone (from Ismetpasa to Sarialan, Figure 1b). Near its eastern ending (Mülayim) the creeping segment crosses an ophiolite mélange that is included within a Trias-Jurassic schist unit.

All the outcrops along the Ismetpasa creeping segment have a common features: near E-W trending vertical faults and shear zones, with evidence of horizontal sliding (striaes) that are associated with thick gouge materials containing clay minerals and showing tectonic layering. The gouge generally has a mineral composition and inner microstructure different from that of the initial rock and the damage zone. In order to best describe these fault rock structures continuously from regional to microstructural scales, we describe in the following the fault zones (damage zone versus gouge) at three different sizes: macro (10–1000 m), meso (1–100 cm), micro (10–1000 μm).

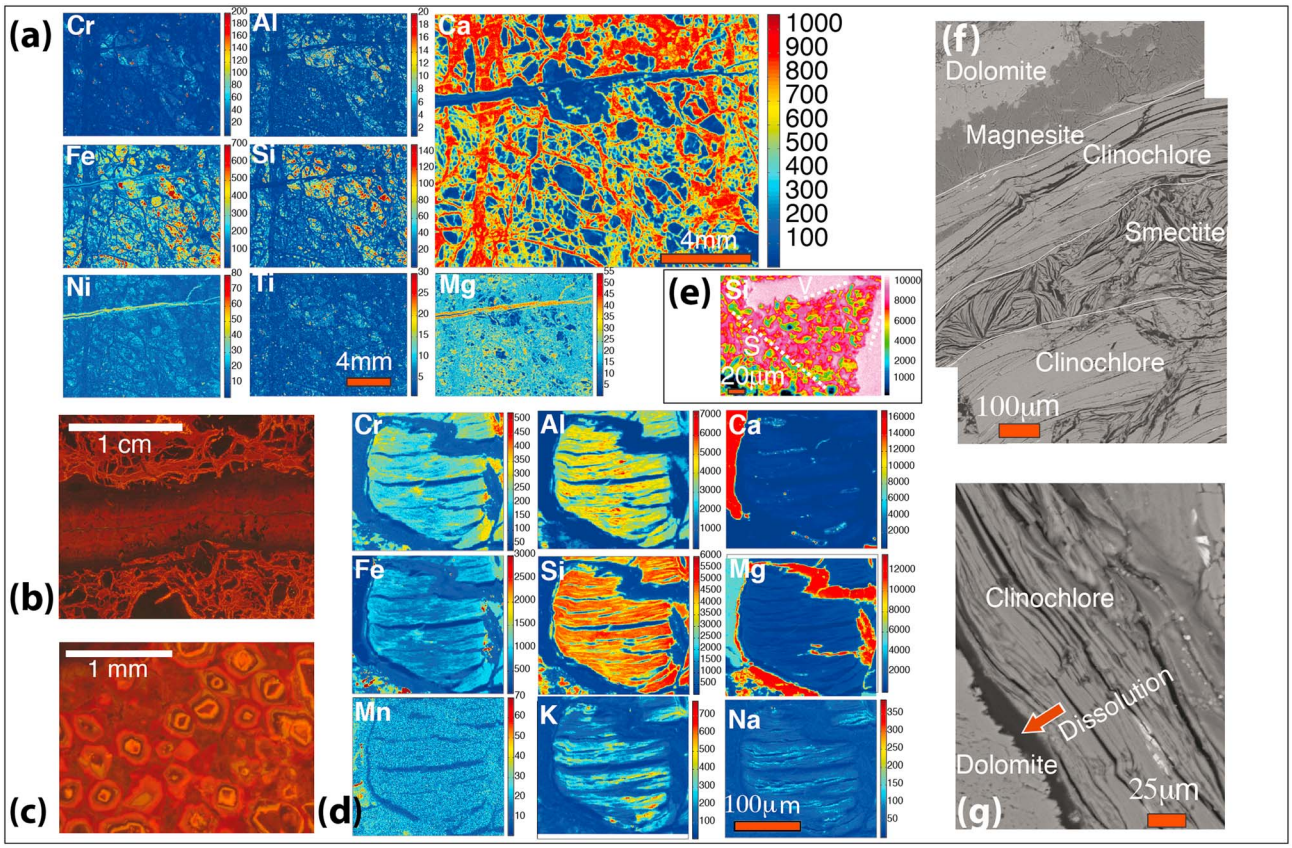

Figure 5. Gerede outcrop: microstructure of the damaged rock (sample G14 in Figure 4c), with initial volcanic rocks intensively sheared and fractured. (a) Chemical map of elements using XRF with typical network of calcite dolomite and magnesite veins parallel and perpendicular to the foliation. (b and c) Cathodoluminescence image of a carbonate veins: (b) magnesite vein crosscutting dolomite veins, indicating several cracking-sealing episodes and (c) calcite crystals with euhedral shape indicating growth in open cavities with fluid flow from depth through seismic faults. (d) Zoom using EPMA chemical mapping showing a cavity filled with chlorite and clay minerals. (e) Quartz veins (V) more or less perpendicular to cleavage (S) in the damage zone (G07 in Figure 4a). (f) SEM image of a vein (G09 in Figure 4a) composed of dolomite and magnesite (top) bounded by layers of clinochlore and smectite (bottom). (g) Stylolite peaks along dolomite vein indicative of stress-driven dissolution, with an orientation in agreement with the main compressive direction along the North Anatolian Fault.

3.2.1. Gerede Outcrop

A fault outcrop near Gerede (Figure 4) is located at the western end of the Ismetpasa creeping segment (Ge, Figure 1b) where the present-day creep rate tends to zero [*Cetin et al.*, 2014]. The fault crosses volcanic units of the Galatia massif, (Mi7 and T7, Figures 4a and 4b) [*Adiyaman et al.*, 2001]. The different units are indistinguishable and contain a mélange of dacite, andesite, and trachy basalts [*Wilson et al.*, 1997]. The outcrop is located in an abandoned quarry on the roadside west of Gerede south of the main faults (Figures 4a and 4b). The initial volcanic rock is highly damaged with fractured blocks and near-vertical veins in all directions. In places, 5 to 50 cm thick clay-rich fault gouges contain very weak material (noncohesive) that can be dug up by hand (Figure 4c).

3.2.1.1. Damaged Rock and Gouge Macrostructure

Thanks to the good exposure of the outcrop, the architecture of the fault zones could be mapped, as well as the spatial distribution of the mineral composition in the fault gouges compared to the damaged rock (sample locations marked by yellow stars in Figure 4a). The main fault contains gouge layers, which have been sampled using metal tubes (Figure 4c). Figure 4d displays the mineralogical composition from XRD analyses of all samples sorted by soluble (and insoluble) mineral contents and their distance to the fault core. A clear spatial variation in the mineralogical composition can be seen, with an abrupt change when passing from the damage zones to the gouges (indicated by the green dashed line in Figure 4d). Most of the damaged rocks contain a large amount (70% to 95%) of carbonate minerals, such as magnesite and dolomite, in veins. The gouge samples contain 60% to 90% of smectite (montmorillonite and saponite) and other insoluble minerals (phyllosilicates and iron oxides).

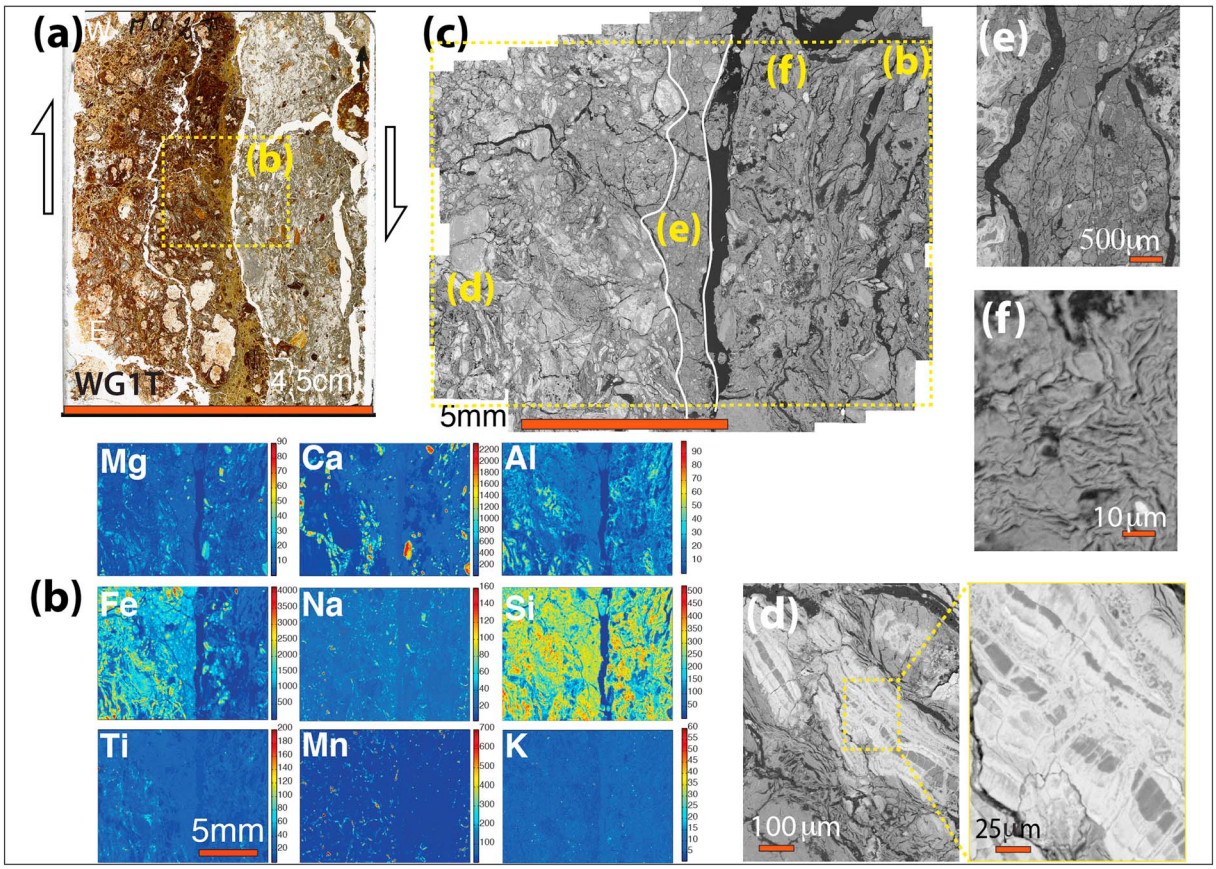

Figure 6. Gerede outcrop: microstructure of the gouge. (a) Horizontal thin section of part of gouge sample G1T (see Figure 4c for sample location) showing a contact between two layers: a brownish-red layer and a gray layer. Arrows are parallel to the strike-slip fault. (b) Map of elements at the contact between the two layers using XRF, showing that the main difference of color between the two gouge layers is due to variations in iron content. (c) Mosaic of SEM-BSE images at the same location with the diffuse boundary (contact layer) attached to the brownish-red layer. (d) BSE image showing Fe-rich carbonate veins parallel to the layering that form a boudinage with Fe-rich carbonate sealing (see details in the enlarged part). (e) BSE image of the boundary zone and (f) typical smectite minerals in the gray layer.

3.2.1.2. Damaged Rock Mesostructure

Centimeter-scale maps of elements measured using XRF show that the typical damaged rock is highly carbonated, as indicated by zones rich in Ca and Mg (Figure 5a). These are veins of dolomite (Ca + Mg) in all directions, crosscut by magnesite veins (Mg) in one direction oblique to the fault. Consequently, there is almost no significant trace of the initial rock containing elements like Si, Al, and Fe. A cathodoluminescence image was focused on a magnesite vein crossing dolomite veins, both vein arrays showing several crack-seal episodes (Figure 5b), as well as cavities filled with euhedral calcite (Figure 5c).

3.2.1.3. Damaged Rock Microstructure

Zooming on damage zones using element EPMA maps shows that between the network of dolomite and magnesite veins, some foliated chlorite minerals remain (Figure 5d). Preserved quartz veins can also be seen (V) more or less perpendicular to the solution cleavage (S) (G07) (Figure 5e). SEM images in Figure 5f show dolomites and magnesite veins locally parallel to alternating layers rich in clinochlore and smectite (G09). The clinochlore layers have a foliated structure, whereas the smectite layers show no clear preferred orientation (Figure 5f). In places, the carbonate veins show rough walls, indicating partial dissolution (Figure 5g).

3.2.1.4. Gouge Mesostructure

Thin sections were prepared from samples taken from the gouge layers in order to study their chemistry and structure. As pointed out previously, here the gouges are formed by layers oriented subparallel to the fault surface (Figure 4c). The thin section made from part of the G1T sample with high smectite content is presented in Figure 6a. This sample is composed of two types of gouge layers that are associated with different structures and minerals: a brownish-red layer, a diffuse boundary (contact zone), which seems attached to the brownish-red layer, and a gray layer. The chemical difference is revealed on the XRF element map (Figure 6b):

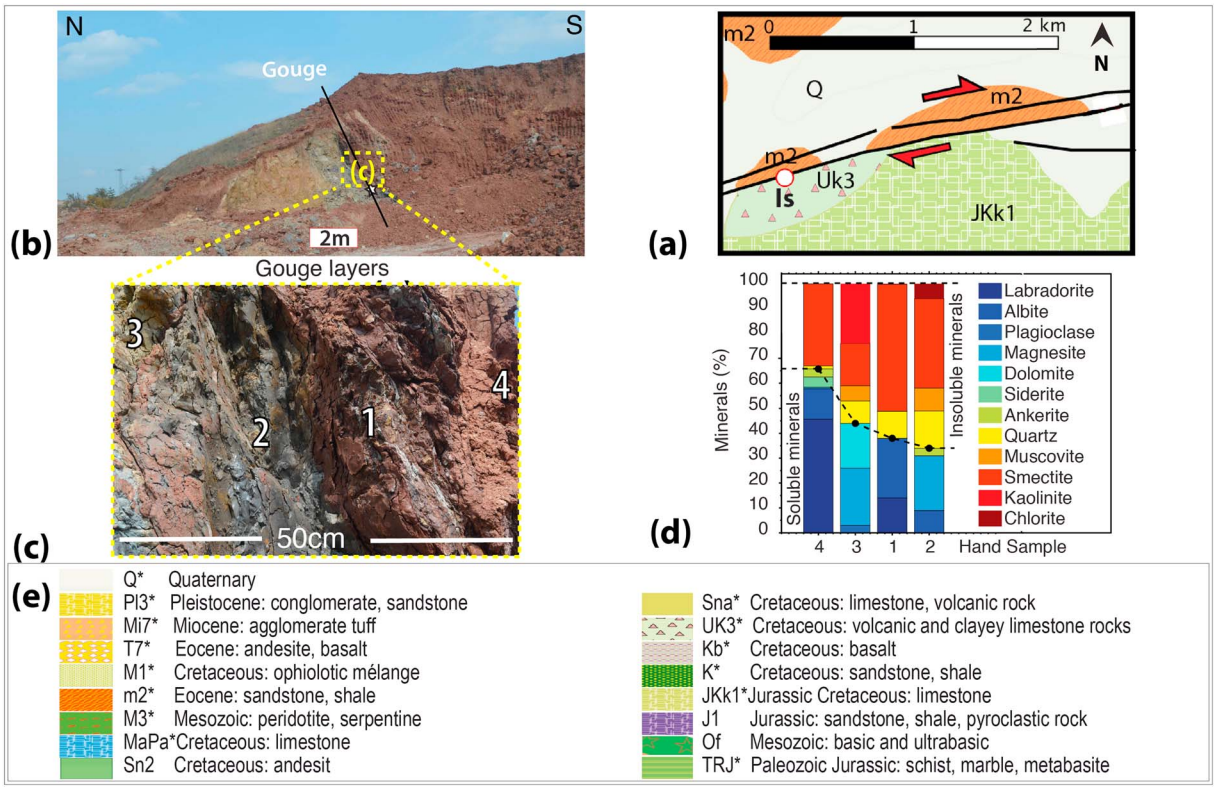

Figure 7. Ismetpasa outcrop: fault gouge with clasts of the initial rock. (a) Geological map (see lithology in Figure 7e). (b) Photograph of the outcrop with the volcanic host rocks and the fault zone containing clay gouge layers. (c) Zoom on the gouge layers (samples 1–3 in Figure 7d) and the damaged rock (sample 4 in Figure 7d). (d) XRD analyses of gouge mineralogy compared to the damage zone; see the supporting information for detailed content. (e) Geological units of the 1/100,000 geological maps [*Herece and Akay*, 2003] of Figures 2, 4, 7, 9, and 12–14. The asterisks refer to units that have been sampled.

the matrix of brownish-red layers is richer in Fe in comparison with the gray layers and is crosscut by Mg-Ca carbonate veins, some also being rich in Fe. A mosaic of BSE images shows the structural characteristics of these zones (Figure 6c). In the brownish-red layer, dolomite clasts (Mg + Ca) appear as boudins that are aligned along curvy layers, while in the gray layer the dolomite clasts are smaller and show a more random arrangement in the smectite matrix.

3.2.1.5. Gouge Microstructure

The brownish-red layers contain carbonate fragments embedded in a clay matrix with a network of Fe-rich carbonate veins parallel and perpendicular to the foliation (Figure 6d). The contact zone is characterized by very small, rounded, granular carbonate fragments embedded in a smectite matrix (Figure 6e). The gray zone comprises fragments of carbonate veins that form small angular fragments spread randomly within the smectite matrix. The smectite matrix may have been disturbed during the thin section preparation process; however, the clay foliation is organized in domains without preferred orientation (Figure 6f).

3.2.2. Ismetpasa Outcrop

This outcrop is located 2.6 km west of the Ismetpasa settlement (Is, Figure 1b), where an active creep rate of 6–10 mm/yr has been measured [*Cetin et al.*, 2014] and where there is clear evidence of creep offset (40 cm) along the concrete wall of a gas station. Recently, a fresh outcrop was excavated (Figures 7a and 7b) for the construction of a water canal and this gives access to the entire fault zone, including the initial rock. An Eocene sandstone-shale unit (m2) on the north side of the fault is in contact with a volcanic rock (Uk3) on the south side. The fault zone in this volcanic rock contains several thin gouge layers, with anastomosing geometry and presence of cleavage. Trails of CO_2 bubbles in a small pond are indicative of active CO_2 circulation along the fault.

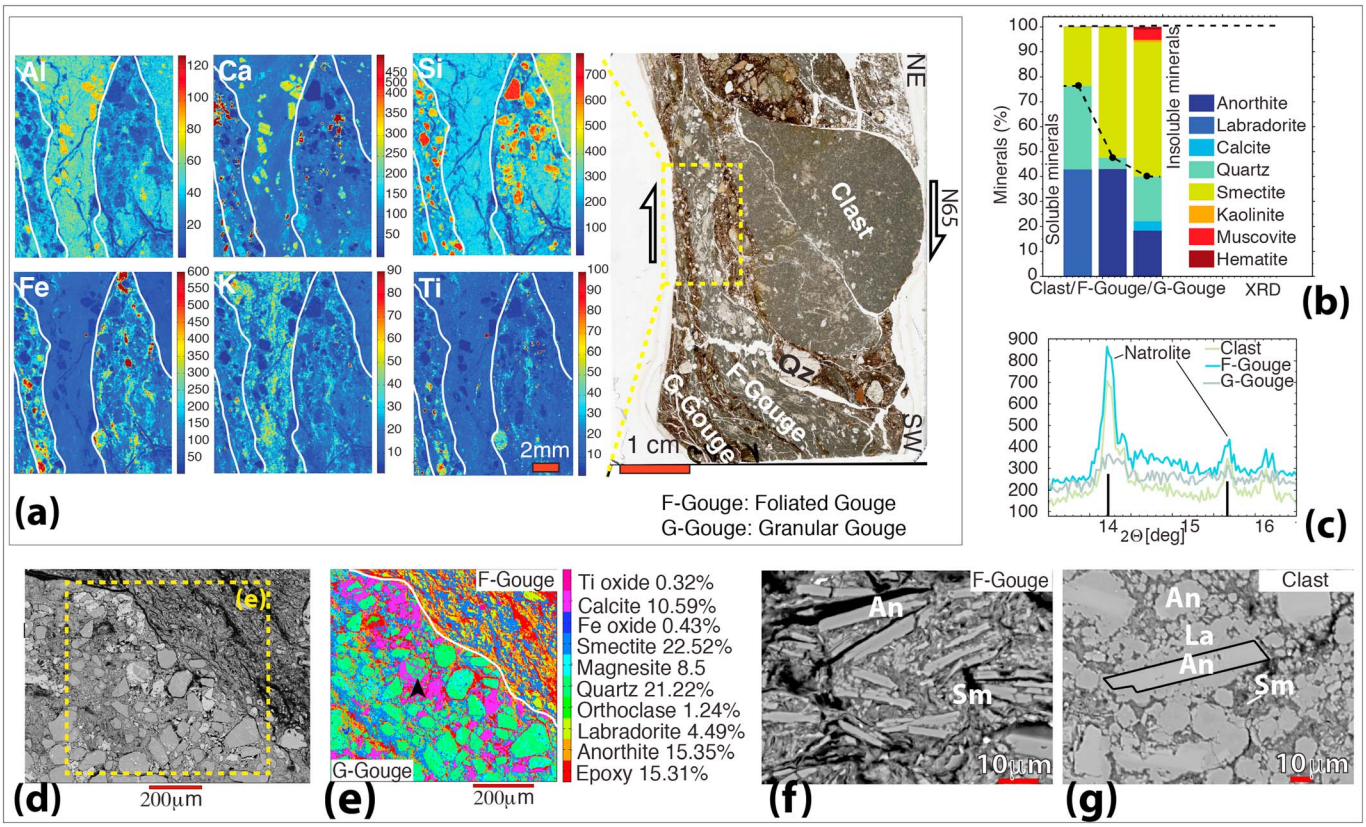

Figure 8. Ismetpasa outcrop: (a) Horizontal thin section (sample 1 in Figure 7c) oriented perpendicular to the strike-slip fault with foliated gouge layers (F-gouge), granular gouge (G-gouge) and a volcanic clast marker of the initial state (right), and XRF maps of the F- and G-gouges (left). (b) XRD quantification of mineral concentrations of those samples reveal that the smectite content is more than double in the gouges compared to the clast. (c) XRD pattern of the clast, F-gouge, and G-gouge with natrolite peak (>1%). (d) SEM image showing the boundary between the foliated gouge and the granular gouge. (e) Mineralogical map from EPMA analysis showing the difference between the granular (bottom) and the foliated (top) gouges; some grains contain crack-seal calcite veins in all directions (arrow) (f and g) alteration of plagioclases: in the foliated gouge, anorthite grains are surrounded by large amount of smectite (Figure 8f) and in the clast anorthite grains are surrounded by labradorite with few smectite around in the clast (Figure 8g).

3.2.2.1. Damaged Rock and Gouge Mesostructure

The site exposes a main fault plane with gouge zones (~25 cm thick) with continuous layering of centimeter to millimeter thickness (Figures 7a–7c). The XRD data of samples taken in and near the gouge (Figure 7d) indicate that the phyllosilicate content (smectite, kaolinite, muscovite, etc.) ranges from ~30% to 50% with variable quartz content. In this case, the soluble (mobile) minerals are plagioclase feldspars.

3.2.2.2. Damaged Rock and Gouge Microstructure

On a thin section oriented perpendicular to the fault plane (Figure 8a), shear zones are deflected around a clast, which is clearly an undeformed piece of volcanic rock and which can be considered as representative of the initial volcanic rock (see Figure 8g) assuming that it was rather homogeneous. The shear zone consists of an alternation of two types of gouges: a granular gouge and a foliated gouge. They can be distinguished by both structure and chemical composition. When comparing the initial rock composition with the composition of these two types of gouge (Figure 8b), the phyllosilicate content (smectite) varies from ~20% to 60%. There is less quartz in the foliated zone than in the granular zone and more feldspars. These samples also reveal a small amount (~1%) of zeolite group mineral (natrolite) (Figure 8g). From XRF and EPMA maps (Figures 8a–8e), the granular gouge is characterized by angular and rounded grains of plagioclases and quartz embedded locally in a carbonate matrix with some thin layers of smectite. Some of the grains show indentation between plagioclase, quartz, and calcite, and some grains contain crack-seal calcite veins in all directions (Figure 8d). The foliated zone comprises much smaller grains of quartz and feldspar embedded in a smectite matrix. SEM observations in this foliated clay gouge (Figure 8f) show the elongated tabular

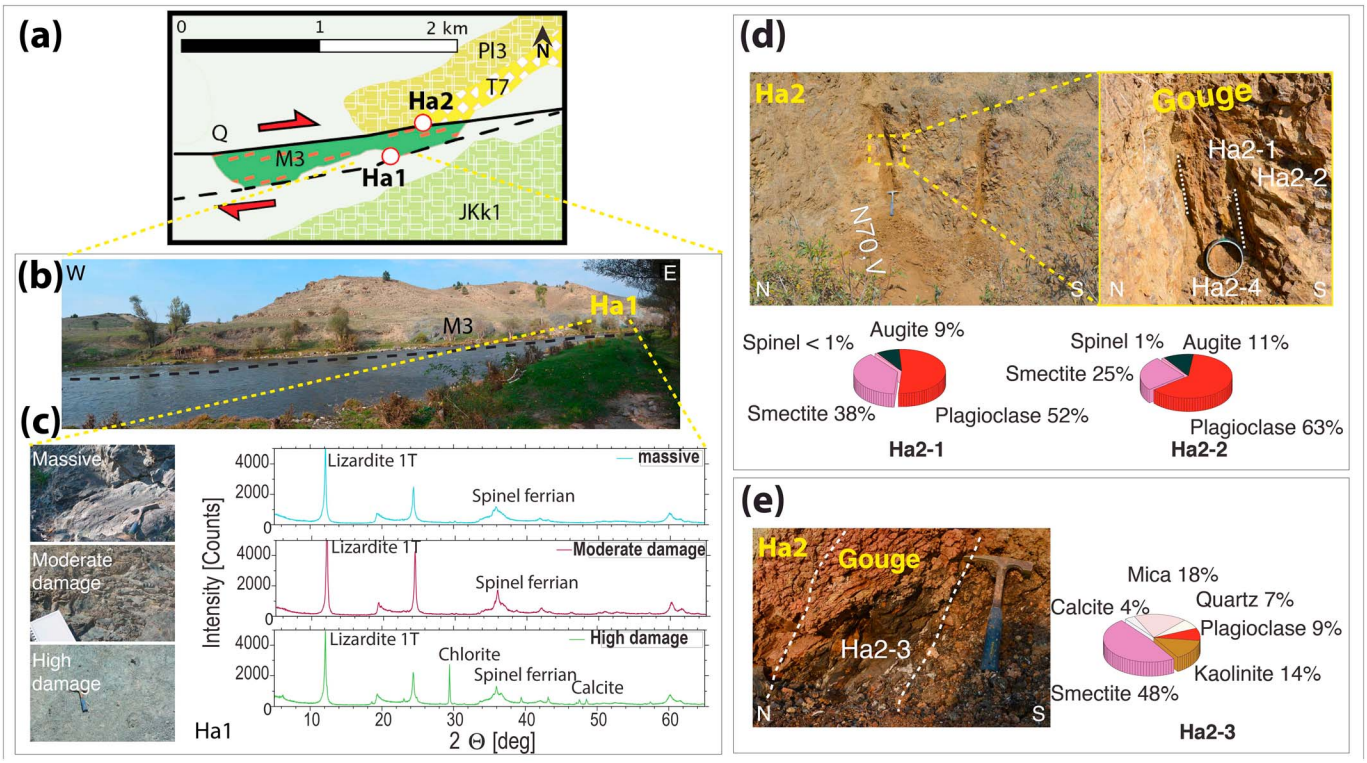

Figure 9. Hamamli outcrops: on minor fault in serpentines, (Ha1 in Figures 9a–9c) and in major fault gouge in volcanic rocks at the contact with serpentines (Ha2 in Figures 9d and 9e). (a) Geological map with sample locations (see lithology in Figure 7e). The main active fault is indicated by a thick black line and is currently monitored by leveling methods that show active creep. A secondary (nonactive) fault is highlighted by a dashed line. (b) Serpentine outcrop along the secondary fault (dashed black line). (c) Zoom on the three types of damaged materials in the serpentine unit and corresponding XRD spectra showing mineral compositions. (d) Gouge and volcanic host rock outcrop; see location in Figure 9a, with layering and mineral composition calculated from XRD data. (e) Gouge, same location as Figures 9d, with anastomosing cleavage and mineral composition calculated from XRD data.

crystals of calcic-plagioclase (with average dimensions ~2 × 10 μm) that are subparallel to the undulated cleavage surface. An interesting change in the plagioclases may be seen when comparing the plagioclases from the clast (anorthite core surrounded by labradorite, Figure 8g) with the plagioclases within the clay gouge (no more labradorite around the core and development of smectite, Figure 8f).

3.2.3. Hamamli Outcrops

These outcrops are located 0.4 km east of the Hamamli settlement (Ha, Figure 1b) where an active creep rate of 5 mm/yr is measured [*Cetin et al.*, 2014]. This area is characterized by the presence of an elongated body of serpentinized peridotites of Mesozoic age (M3, Figure 9a) and has been studied by *Dor et al.* [2008] and *Ozakin et al.* [2012].

This serpentine body along the North Anatolian Fault is in contact with a volcanic unit to the north (T7) and a Jurassic limestone unit to the south (JKk1) lying under quaternary cover. On this site, the focus was placed on two outcrops along two faults: the first (Ha1) on a minor fault in the serpentine and the second (Ha2) on the major fault gouge in the volcanic rock at the contact with serpentine units (Figure 9a). This was a good opportunity to compare the behavior of serpentine with volcanic gouge.

The first outcrop, Ha1, along the minor fault (Figure 9b) exposes serpentine rocks with anastomosing polished surfaces and evidences of shear deformation. At the outcrop scale the variations in damage intensity are spatially heterogeneous: the serpentine shows three kinds of damage, from slight and pervasive to moderate and intense (Figure 9c). The main compositional difference is that the highest deformed serpentines contain more chlorite and calcite than the least deformed ones (Figure 9c).

The second outcrop, Ha2, along the major fault, shows a gouge in volcanic rocks (T7) near the contact with the serpentine body M3 (Figure 9a).

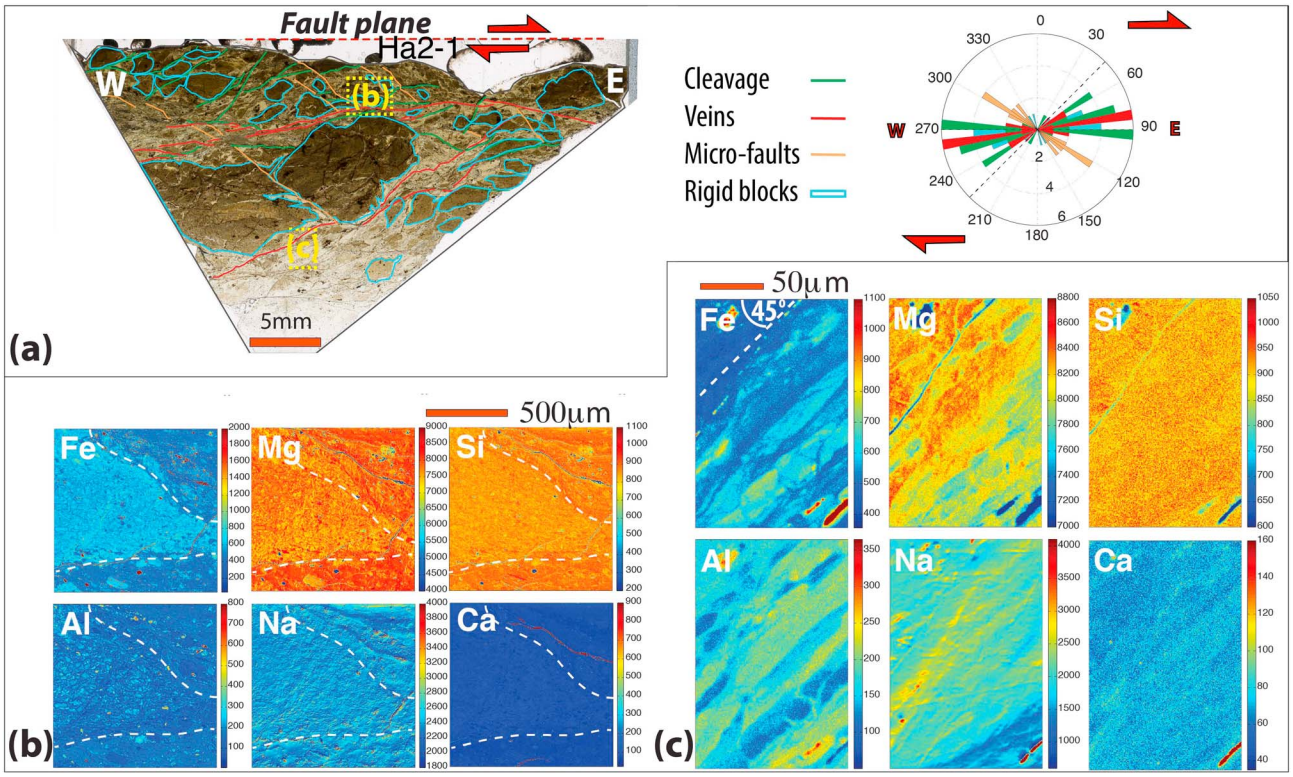

Figure 10. Hamamli outrops: damage zone near the fault gouge (Ha2). (a) Horizontal thin section of damage zone near the gouge (Ha2-1), perpendicular to the strike-slip fault shown in Figure 9d, with segmentation of veins, cleavage, microfault, and rigid blocks whose relative orientations are indicated in the rose diagram. (b) XRF map, located on the thin section, showing rigid block with a mesh texture and parallel-to-layering siderite vein. (c) EPMA chemical maps, located on the thin section, showing tectonic layering oblique to the fault.

3.2.3.1. Gouge Mesostructure

The XRD measurements (Figures 9d and 9e) show the variation in composition from damaged rock to gouge, with smectite content increasing from 25% in the damaged rock (Ha2-2) to 38% in a transition zone (Ha2-1) and up to 48% in the gouge (Ha2-3), with feldspar content decreasing accordingly.

3.2.3.2. Damaged Rock Microstructures

A thin section (Ha2-1) located at the transition between damaged rocks and gouge (Figure 9d) shows a cleavage angle ranging from 0 to 45° with respect to the fault direction with sets of microfaults at about 30° from the fault, as in C-S shear structure (Figure 10a). Shear deformation can be distinguished by alignments of iron oxides that reflect tectonic layering corresponding to the cleavage with rigid blocks surrounded by more deformed zones. The contrast in mineral composition of these zones can be seen on XRF map (Figure 10b), with veins of siderite parallel to the cleavage. EPMA maps of elements across the shear zone (Figure 10c) also show the compositional tectonic layering oblique to the fault at smaller scale.

3.2.3.3. Gouge Microstructures

A thin section of gouge (Ha2-4, Figure 9d) reveals two rich-in-clay shear zones, 100–200 µm wide, with a high degree of deformation oriented obliquely to the fault (Figure 11a), where the grain size is smaller than 30 µm. Given the very small grain size, it is difficult to quantify the change in element distribution along the deformation zones from XRF maps. However, the high deformation zones are depleted in Ca and enriched in Fe and K. The network of fractures both parallel and perpendicular to the high deformation zones contains carbonate minerals rich in Mn (Figure 11b). Of the two high deformation zones, one contains localized cataclastic damage with distinct boundaries (Figure 11d), while the other is more diffuse. Two types of elongated calcite bodies can be observed in places that are subparallel to this second high deformation zone. The first type corresponds to compact veins that show dissolved edges adjacent to microstylolites (Figure 11e); the second type takes the form of clusters of grains and is associated with iron oxides (Figures 11f and 11g).

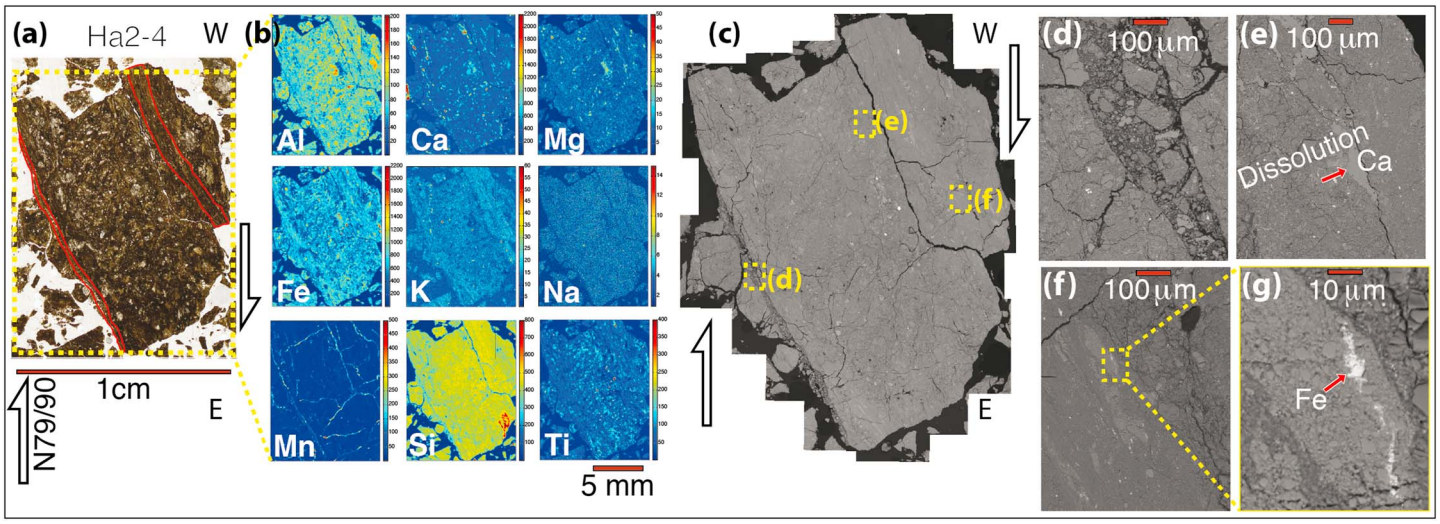

Figure 11. Hamamli outcrops: along the main fault gouge (Ha2). (a) Horizontal thin section of a gouge core Ha2-4 (see location Figure 9d; arrows are parallel to the strike-slip fault), with two shear zones (in red) oblique to the fault. (b) XRF map of elements showing the layering. (c) SEM-BSE panorama with three selected zones: (d) cataclastic band, (e) tectonic microstylolite oblique to the fault, dissolving calcite vein, and (f) calcite aggregates forming elongated clasts along horizons subparallel to the cataclastic bands. (g) Located in Figure 9f; in places some of the calcite clasts are associated with iron oxides.

3.2.4. Yazioren Outcrop

Near Yazioren the present-day creep rate is 6 mm/yr in average [*Cetin et al*., 2014]. In this zone, the fault is more diffuse and forms a large shear zone [*Ellero et al*., 2015]. The outcrop (Ya, Figure 1b) is located on the roadside about 1 km southwest of Yazioren village in volcanic and clayey limestone rocks (Uk3, Figure 12a). It shows an ~20 m shear zone with metric to decimetric width localized anastomosing cleavage (Figure 12b). Unfortunately, in view of the limited exposure, it was not possible to compare the composition of the shear zone with that of the initial rock. Unlike the other outcrops, it is not easy to distinguish between damaged rock and gouge. However, zones with anastomosing cleavage were investigated. The mean mineralogical composition of the rock indicates a mélange of carbonate and volcanic minerals, with 36% of mica.

3.2.4.1. Gouge Mesostructure

In the thin section Ya2 (Figure 12c) there is a clear structural and mineralogical separation between two types of layers. The first type of layer is made of carbonate-rich material mainly composed of calcite, dolomite, gypsum, and quartz grains (so-called calcitic-silicate layer). The layer elements are disrupted and form a boudinage with pinch-and-swell structure where the open voids developed between the boudins are sealed by calcite. The second type of layer is rich in muscovite, chlorite, albite, and anatase (so-called aluminosilicate layer). XRF maps of elements (Figure 11d) show the oblique-to-the-fault foliation (40–60°) that has been locally rotated near a small shear zone parallel to the fault. They also highlight the contrasting composition of calcitic-silicate layers and foliated aluminosilicate layers with calcite sealing of the interboudin veins.

3.2.4.2. Gouge Microstructure

The mosaic of SEM images shows the microstructures of the two types of layers. Figures 12e and 12f focus on a zone with an aluminosilicate layer that is confined between two calcitic-silicate layers. Here the upper calcitic-silicate layer is more disrupted and fractured compared to the aluminosilicate layer. Calcitic-silicate layers deform by extension due to boudinage with carbonate sealing and contraction due to stylolitization of the boundary (Figure 12f). They are composed of large closely entangled grains of quartz in a calcite vein network with dissolution at grain boundaries (Figure 12g). In contrast, the aluminosilicate foliated layer (Figure 12h) contains smaller grains of different minerals (quartz, calcite, plagioclase, mica, chlorite, Ti and Fe oxides, etc.) that have been deformed by the dissolution of the smaller grains of quartz and feldspars. This is attested by the passive concentration of the more insoluble phyllosilicates and oxide minerals in the solution cleavage planes. Another thin section Ya3 (Figure 12i) shows an example of a layer that has been completely disrupted, as a result of rotations that have formed rolling clasts between a boudinage of layers. The contrast of deformation behaviors between polymineralic and monomineralic materials is clearly apparent here and on other thin sections. Polymineralic layers corresponding to foliated layers show dissolution of

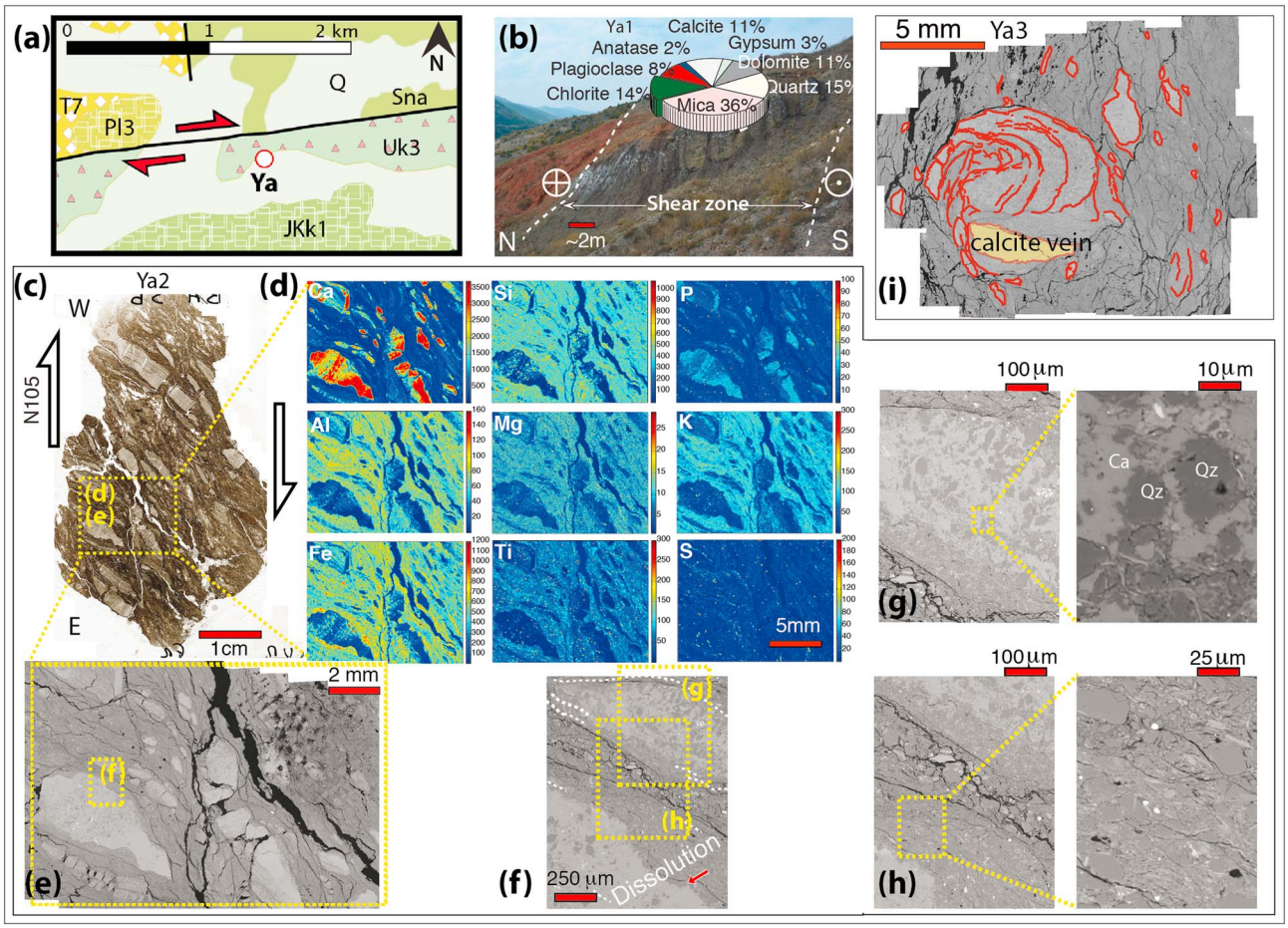

Figure 12. Yazioren outcrop: shear zone. (a) Geological map with outcrop location; see lithology in Figure 7e. (b) Shear zone, ~20 m wide, with composition in a deformed zone shown in the pie diagram. (c) Horizontal thin section (Ya2) showing a boudinage of carbonate layers with stylolitic boundaries. Arrows are parallel to the strike-slip fault. (d) XRF maps of elements showing the foliation layering. (e) Mosaic of SEM images. (f) Zoom in between the layers with microstylolites at the boundary of the clast. (g) Detail of calcitic-silicate layers and zoom on grain indentations between quartz and calcite. (h) Detail of aluminosilicate foliated layer and zoom showing that some stronger minerals (plagioclase and quartz) are embedded in the clay. (i) Horizontal thin section (Ya3): tightly folded layers overprinted by a rigid calcite vein.

quartz and feldspar at grain scale (Figures 8b–8e) and are folded (Figure 12i), whereas the massive monomineralic calcitic veins, which cut the boudins or the rolling layers of clasts, are, in general, undeformed (Figures 12d and 12i). The only deformation that is seen for such monomineralic veins and for the others dispersed in the matrix is the dissolution at their boundaries (Figures 12f, 12g, and 12i).

3.2.5. Sarialan Outcrop

This outcrop (Sa, Figure 1b) is located in an area where an average creep rate of 8 mm/yr is measured [*Cetin et al.*, 2014] in volcanic rock (Uk3), in contact with a sandstone-shale unit (K) north of the fault Figure 13a. The fault contains a foliated gouge composed mainly of aluminosilicates, with 41% of mica and 24% of kaolinite (Figure 13b).

3.2.5.1. Gouge Mesostructure

The thin section Sa1 (Figure 13c) shows two types of layers: one with a dense array of quartz grains and the other one with isolated small quartz grains embedded in a foliated aluminosilicate matrix. XRF maps of elements focused on the contact zone between these two layers (Figure 13d) show that the quartz-rich layers are fractured, with some veins sealed by calcite. The foliated zone shows thin layering underlined by the variations in Al and K contents.

3.2.5.2. Gouge Microstructure

A SEM-BSE panorama shows the differentiation between quartz-rich and aluminosilicate-rich layers (Figure 13e). Zooming on the aluminosilicate-rich layers, which contain illite, kaolinite, small amounts of

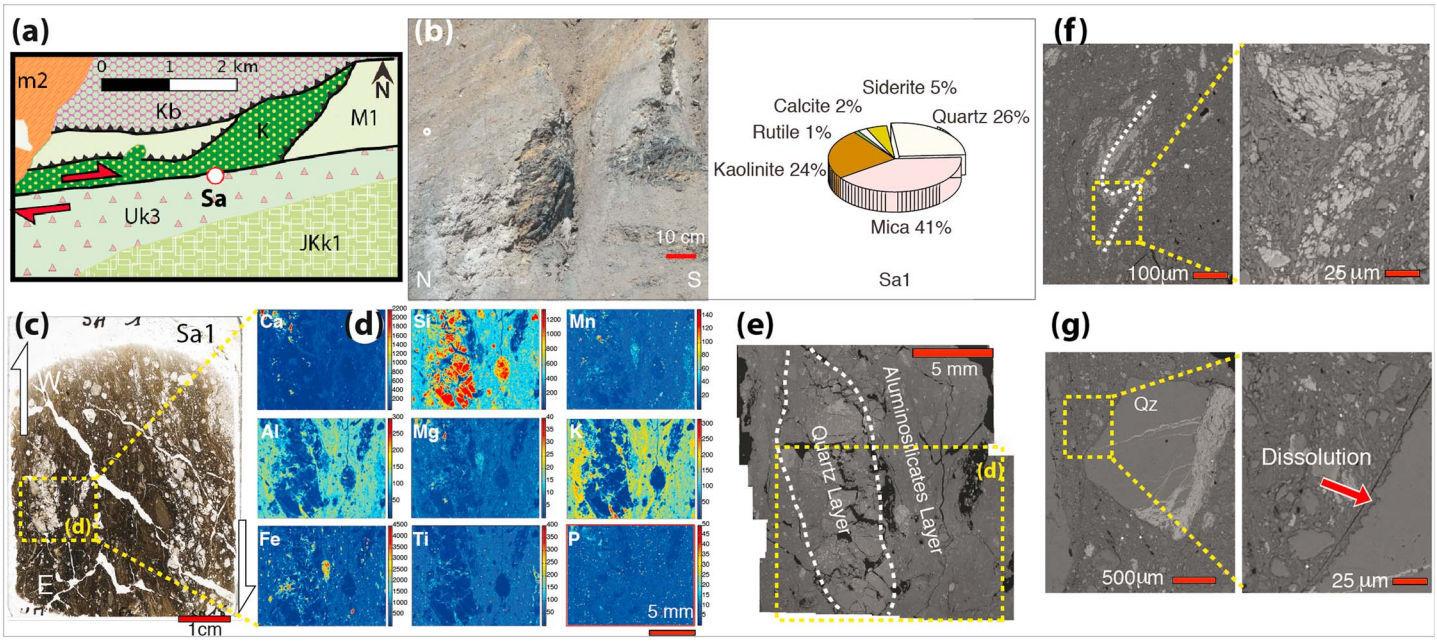

Figure 13. Sarialan outcrop: fault gouge. (a) Geological map (see lithology in Figure 7e). (b) Outcrop with mineral content. (c) Horizontal thin section Sa1 in the vertical E-W gouge: arrows are parallel to the strike-slip movement. (d) XRF maps of elements showing the foliation layering: arrows are parallel to the strike-slip fault. (e) SEM_BSE panorama. (f) Detail of folded layers: the zoom shows the rotation of elongated plagioclase minerals. (g) Quartz grain with dissolved edges and carbonate veins.

quartz, and some rare albite, shows that these layers are folded, with the long axis of the mineral grains parallel to the folded layers (Figure 13f). In the quartz-rich layer the quartz fragments have rough dissolution boundaries (microstylolites), and the fractures are filled with iron-rich carbonate minerals (Figure 13g).

3.2.6. Mülayim Outcrop

This outcrop (Mu, Figure 1b) is located in an area where the measured creep rate is close to 6 mm/yr [*Cetin et al*., 2014]. It is located on a riverbank where the fault crosscuts a block of ophiolitic mélange (M1) within schists, marbles, and metabasite units (TRJ). Here as in other examples, tectonic layering can be observed both in the gouge and in the nearby damaged rock (Figure 14b).

3.2.6.1. Gouge Mesostructure

XRD analysis shows the composition of the gouge from its core to its boundary (Figure 14c). The thin section Mu1 shows layers subparallel to the fault (Figure 14d). The XRF maps indicate layering at various scales cross-cut by carbonate veins in all directions (Figure 14e). Three types of carbonate veins appear on the Ca map: (i) veins oblique or perpendicular to the layers, (ii) tightly folded veins with millimeter wavelength, and (iii) veins parallel to the layers.

3.2.6.2. Gouge Microstructure

SEM-BSE images (Figure 14f) also show tightly folded thin carbonate veins and the growth of mineral sealing in veins parallel and oblique to the foliation (Figures 14i and 14j). Alternations of weak and strong layers are seen with a mix of clay and phyllosilicate with small grains of plagioclases, mica, chlorite, and quartz in the weak zones (Figure 14g) and large grains of plagioclase and quartz sealed with dolomite in places mixed with carbonate veins with dispersed phyllosilicates in the strong zones (Figure 14h).

3.2.7. Common Characteristics

In summary, five main observations can be made regarding these outcrops along the Ismetpasa right-lateral creeping segments (Figures 4–14).

1. The displacement along the fault is associated with the progressive development of wide shear zones (of hectometric width) that comprise gouge zones (of centimeter to meter width) embedded into wide damage zones (hectometric in width). The gouges are characterized by the development of

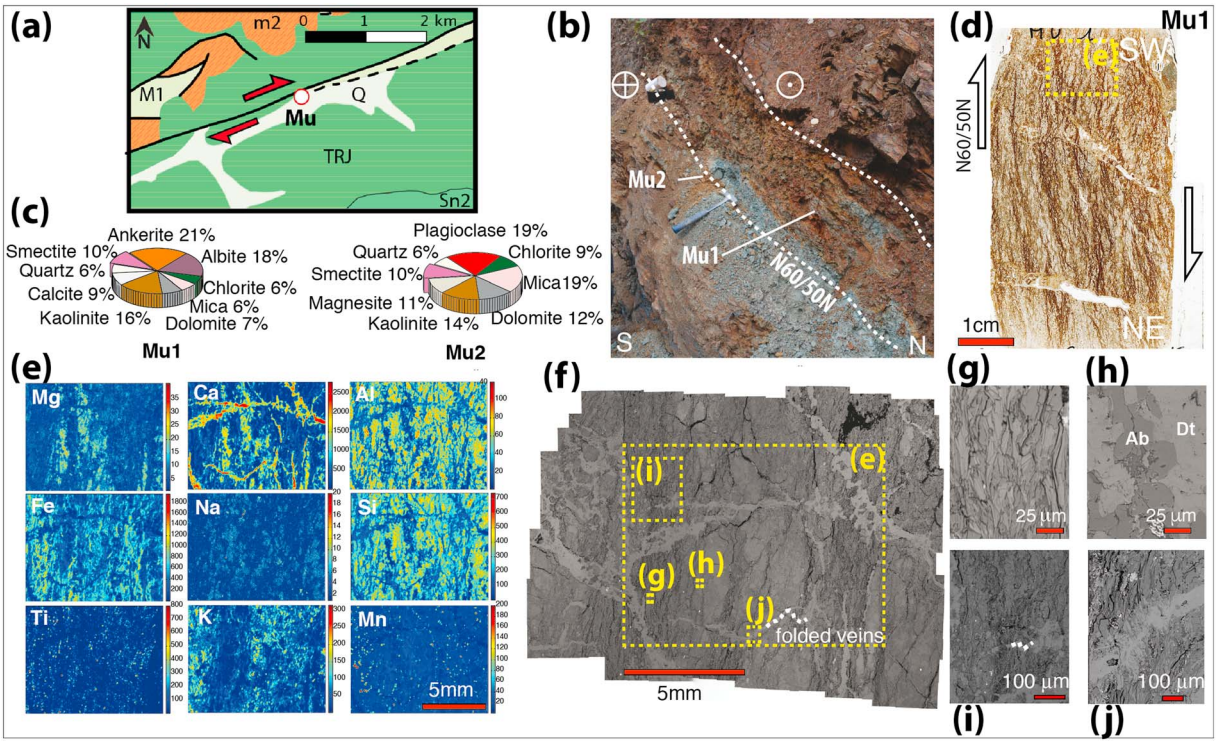

Figure 14. Mülayim outcrop: fault gouge. (a) Geological map (see lithology in Figure 7e). (b) Outcrop with gouge and sample locations. (c) Mineral content. (d) Horizontal thin section Mu1 with tectonic layering and carbonate veins, arrows parallel to the strike-slip fault. (e) XRF maps showing mineral differentiation between the layers crosscut by calcite veins. (f) SEM-BSE panorama showing the layered structure associated with thin folded veins. (g) Weak layer with small grains of plagioclase, quartz in a phyllosilicate matrix. (h) Strong layer composed of albite (Ab) and dolomite (Dt). (i) Detail of thin folded calcite veins. (j) Detail of the growth of the mineral sealing in veins parallel and oblique to the foliation.

pressure solution cleavage and foliation, whereas the damage zones show numerous fractures sealed by carbonates.

2. Comparative chemical analysis of the damage zones and the gouges versus the initial rocks show a drastic evolution with time. The gouges are depleted of the soluble minerals such as quartz and feldspars and passively enriched in the less soluble minerals such as phyllosilicates and Fe and Ti oxides. By contrast, the damage zones are enriched in carbonate up to such content (90%) that it is often difficult to recognize the initial rocks.
3. Various markers of ductile deformation associated with cleavage development such as rolling clasts, asymmetrical folds, and cleavage planes at various angles to the main slipping zone that evolve to fine-grained layers attest of an early ductile behavior of the damage zones before their strengthening by fracture sealing and the concomitant development of localized soft gouges.
4. Cataclastic gouges and intense networks of carbonates veins with euhedral mineral growth that reflect fast void openings attest of seismic events that must have affected the damage zones at an early stage of the fault initiation and opened paths for large carbonated fluid flows coming from outside the fault.
5. Finally, at grain scale, two specific processes can be observed: (i) the metamorphic transformations of phyllosilicates and some feldspars that evolve into clay minerals and (ii) the contrasted behavior of monomineralic rocks that are very difficult to dissolve except at their boundaries by comparison with polymineralic rocks that are much more easily transformed by stress-driven mass transfer processes.

4. Discussion

All observations and measurements presented above allow discussing the characteristics of gouge formation, evolution, and mineral alteration as well as their implications for the creep behavior of the Ismetpasa creeping segment of the North Anatolian Fault. We address in particular the following points: (1) the spatial correlation between the observed present-day creep behavior and the mineral composition of the gouge;

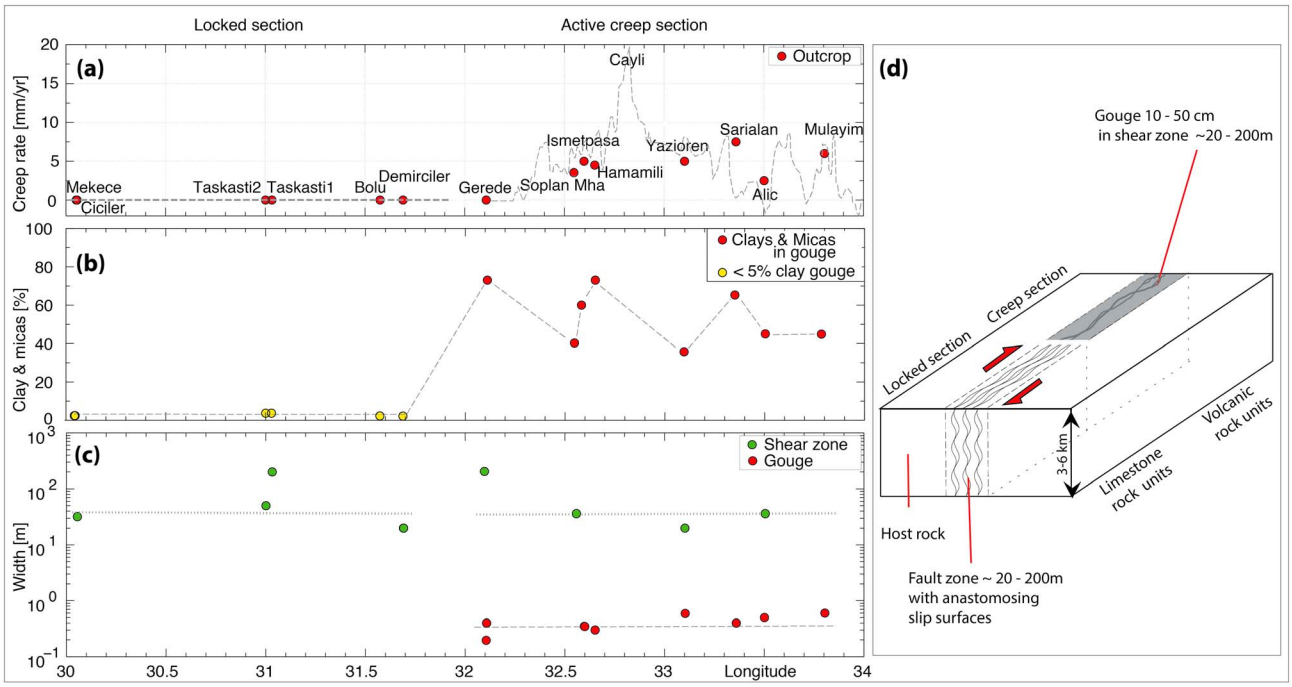

Figure 15. Comparison of locked and creeping zones: (a) Creep rate versus longitude along the North Anatolian Fault from *Cetin et al*. [2014]. The red points indicate the available outcrops where the fault zone is clearly visible in the field and where samples were collected (see Figure 1 and supporting information for locations). (b) Amount of clay and mica minerals in the gouge versus the longitude along the fault. Note the abrupt change in clay and mica content between the locked (limestone units) and the creeping (volcanic units) segments. (c) Width of shear zone or gouge versus the longitude showing the drastic change between limestone and volcanic rocks. (d) Sketch representing the locked segment with a wide shear zone and anastomosing slip surfaces hosted in the limestone rock unit, while the creeping segment has a limited number of branches of localized gouge in a similarly wide shear zone hosted in volcanic units.

(2) the mechanisms of mass transfer, segregation and layering at various scales, and the time-dependent change in fault zone mineralogical and structural properties; (3) the mechanisms of metamorphic mineral transformations that contribute to the creeping processes; and (4) the mechanisms of the aseismic creeping processes.

4.1. Spatial Correlation Between Creep and Gouge Mineral Composition

In the past decade, a considerable amount of data has been collected from experiments, drilling projects, and field studies, showing that the frictional properties of rocks are dependent on the type of minerals, mineral content of the gouge, and water content [*Carpenter et al*., 2011*; Lockner et al*., 2011*; Carpenter et al*., 2016]. Furthermore, experiments on a synthetic clay gouge show that an almost negative linear trend exists between the amount of clay content and the coefficient of friction [*Samuelson and Spiers*, 2012]. Experimental data show that the presence of saponite has a weakening effect, due to low friction $\mu \approx 0.1$ [*Lockner et al*., 2011*; Mittempergher et al*., 2011*; Carpenter et al*., 2011]. The pure muscovite gouge exhibits a higher friction coefficient $\mu \approx 0.3$. This coefficient becomes much higher, up to 0.8, if the sample contains pure quartz or calcite [*den Hartog et al*., 2013] or differing amount of strong minerals [*Bullock et al*., 2015, and references therein]. Hence, it is important to understand the nature of the interplay between creep and mineral composition of the gouge.

Figure 15a shows the creep rate along the North Anatolian Fault measured by *Cetin et al*. [2014]. The maximum creep rate value has been measured in the vicinity of the Cayli settlement (although this maximum value has been revised to a lower rate by *Hussain et al*. [2016b]) and is close to the present-day relative motion of 22 ± 5 mm/yr between the Anatolian and European Plates [*Reilinger et al*., 2006]. In order to compare the gouge composition with the creeping rate along the fault, the amount of clay and mica minerals in the gouges was plotted with respect to longitude (Figure 15b). The locked segments appear as a deformation zone with width in the range 20–200 m (Figure 15c) that contain numerous fractures and cataclastic zones and very thin mirror-like slip surfaces (Figure 2) that are considered as indicative of fast (seismic) sliding

[*Fondriest et al*., 2013]. It has been suggested that such features may also develop at lower sliding [*Verbene et al*., 2014]. However, the observed high Fe oxide content along these mirror-like faults, which could result from decarbonation process that passively concentrated Fe oxides due to carbonate dissociation [*Rowe et al*., 2012, *Collettini et al*., 2013], is also in favor of seismic behavior. In overall, the gouges have almost the same composition as the limestone rocks containing less than 5% of clay minerals. Finally, it must be noted that when canceling the 80 km offset of the fault, the locked segment shows on both sides units of limestone and carbonate clastics since the initiation of the fault (see section 3.1 and Figure 1b).

Conversely, the Ismetpasa creeping segment appears as composed of gouge branches with width in the range 10–50 cm in sheared and fractured damage zones of 20–200 m width (Figure 15c). Along this creeping segment a dramatic change in gouge composition is seen with respect to the locked segment with high clay contents (smectite and kaolinite, as well as other phyllosilicates such as micas, ranging from 40 to 80%, Figure 15b). The gouges are within volcanic units. They result from transformations under stress in actively deforming zones (Figures 6–8 and 10), and such changes are discussed in more details in the section 4.2 below. Note that although there is a clear correlation between the existence of creep and the clay content, the correlation between the creep rate and the clay content is not perfect. For example, the Gerede zone, with a maximum clay and mica content, is located near the west end of the creeping segment where creep rate is small. However, it is not completely certain that we sampled the most present-day active creeping zone. Several parallel creeping zones were often observed in the field (Figure 4a). Moreover, the creeping zone may shift after earthquakes, as observed in the San Andreas Fault (SAF) where the SAFOD drilling project revealed two localized actively creeping zones, 50–200 cm thick, 100 m apart, containing saponite [*Lockner et al*., 2011*; Hadizadeh et al*., 2012], one sliding much faster than the other. Another major limitation of our study along the NAF is that based on geological outcrops alone, it is not possible to properly characterize the geology and mineralogical composition of the gouge of the fault at depth. This is important because gouge composition can change with depth by mineralogical transformation and alteration [*Chester et al*., 2004*; Scholz*, 2006]. Such changes can be crucial for creep behavior [*Richard et al*., 2014]. At the present time, there are no deep drilling data available on the Ismetpasa creeping segment of the North Anatolian Fault. So one can only conclude that there is an overall correlation between the gouge composition observed near the surface and creep, as locked segments do not contain a significant amount of clay and mica minerals and no saponite and montmorillonite, whereas the gouge along the investigated creeping segment contains large amounts of these minerals. However, due to the regional uplift in the area [*Yildirim et al*., 2011], we can reasonably assume that the sampled rocks in the gouge gather samples deformed at various depths, from the surface to several kilometers deep. Finally, one must note that at the present day, the offset of the NAF has put volcanic units and limestone units face to face in some place along the Ismetpasa segment (see section 3.2). However, if the 80 km total offset is canceled, the whole volcanic unit of the Galatia massif in the southern compartment of the fault becomes face to face with its northern volcanic part. This indicates that at the beginning of the transformation of the creeping fault segment the volcanic units where face to face and the creeping process initiated and developed in a volcanic unit.

To summarize, at shallow depth (upper 0–6 km), the locked segments are characterized by an absence of present-day creep and a wide seismic deformed zone with anastomosing slip surfaces hosted in limestone rocks without clay gouges. Conversely, the Ismetpasa creeping segment is characterized by creep rates up to 20 mm/yr and localized clay gouge bands in shear zones hosted in volcanic units (Figure 15d). Due to the uplift and associated erosion processes of the NAF fault rocks [*Yildirim et al*., 2011], the mechanisms observed on the outcropping samples are representative of most of the creeping zone at depth.

4.2. Mechanisms of Mass Transfer, Segregation and Layering at Various Scales, and Time-Dependent Change in Fault Properties

Major faults such as the NAF are likely to act as major fluid channel pathways and zone of fluid rocks reactions. We have described in section 3 several circumstantial evidences of this presence and effect of fluids that are further discussed below. From a general point of view, in natural deformation, mass transfer occurs by two types of mechanism: diffusion through a fluid phase driven by chemical potential differences and advection by fluid flow driven by hydraulic gradients. According to the experiments of *Ildefonse and Gabis* [1976], the maximum distance of diffusive mass transfer over geological times is limited at best to a few meters in the case of mass transfer through a free fluid phase (fluid in open fractures, for example).

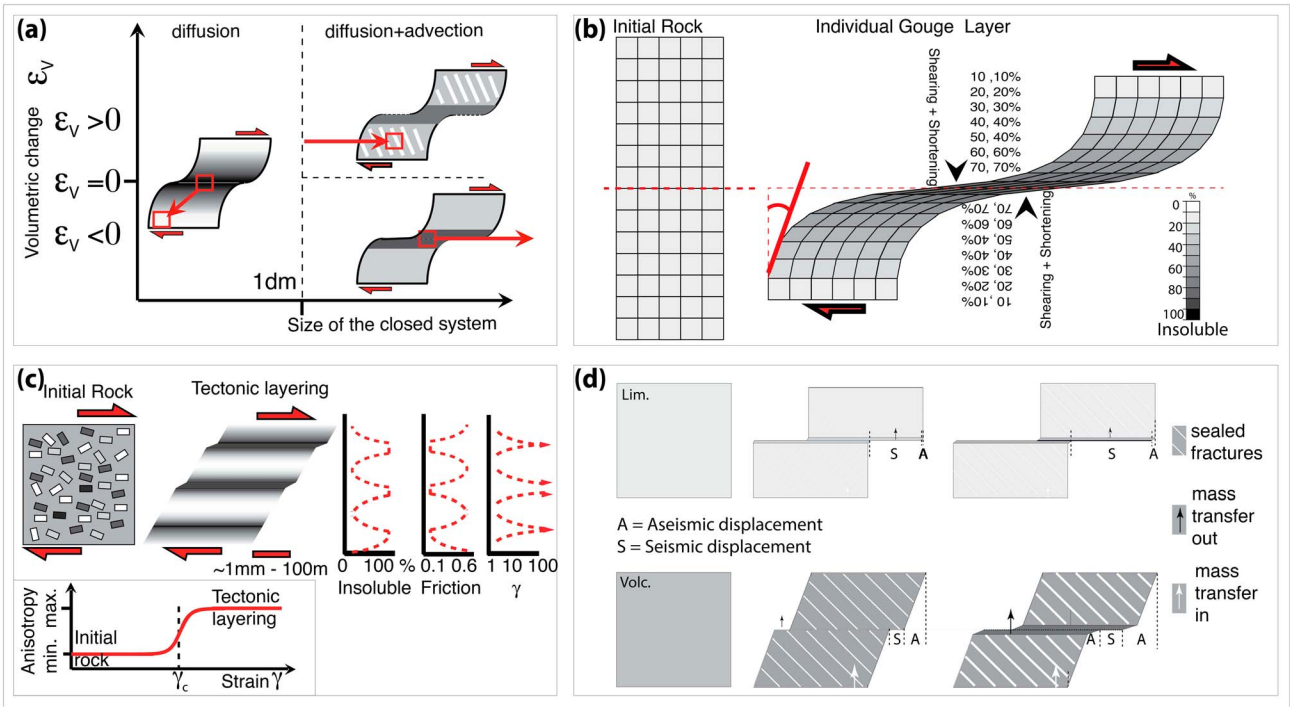

Figure 16. General concepts of tectonic layering and rock transformations. (a) Three types of mass transfer in a diagram showing volume change versus mass transfer distance: mass transfer by diffusion in a closed system over a distance of less than a decimeter (left) and coupled diffusion-advection over greater distances (right) with either a volume gain (veins in damage zone, top) or volume loss (dissolution in the gouge, bottom). (b) Model of passive concentration of insoluble minerals (black) in shear zone with volume loss. (c) Model of tectonic layering development at all scales after critical shear strain, leading to anisotropic rocks with alternations of strong and weak material, with high/low friction coefficient and low/high accommodation of shear strain, respectively. (d) Contrast in limestone and volcanic rocks deformation: limestone deforms by seismic displacement (S) with only very minor postseismic aseismic displacement (A) (top) and volcanic rock deforms by both seismic (S) and aseismic (A) displacement associated with a chemical change in the rocks with mass transfer in and out of the fault zone, leading through time (from left to right) to gouge softening and damage zone strengthening (bottom).

However, most of the time in deformed zones diffusive mass transfer occurs along reactive fluid phases that are trapped under stress at grain boundaries, or in stylolites, or in cleavage planes [*Wheeler*, 2014]. In such cases, the diffusion paths are very thin (see below) and the maximum distance of diffusive mass transfer is reduced to values ranging from a few decimeters to a few centimeters or even less. Mass transfer may occur in closed or open systems. The system is closed if the amount of dissolution is equal to the amount of redeposition and the total solid mass is conserved. Otherwise, the system is considered to be open and the initial rock can lose or gain volume as a result of transport of mobile elements.

4.2.1. Mass Transfer at the Grain Scale

At the grain size scale (μm-mm), various models are used for fluid phases trapped along grain boundaries, from very thin continuous phases to clouds of fluid inclusions. However, the diffusive path width is sufficiently small to be the controlling factor of pressure solution or metamorphic reactions in nature [*Rutter*, 1976*; van Noort et al*., 2008*; Gratier et al*., 2013a*; Wheeler*, 2014]. This explains the observed main difference between monomineralic rocks and polymineralic rocks. Monomineralic rocks do not deform at grain scale in the locked segment (Figure 3) and are hardly deformed at grain scale in some parts of the creeping zone except by dissolution along microstylolites at veins (Figures 11e, 11f, and 12d–12i) or quartz clasts boundaries (Figure 13g). Conversely, polymineralic rocks in the creeping segment show very efficient dissolution at grain scale leading to the dissolution of a large part of the more soluble grains (Figures 8a, 8b, 8e, 9d, and 9e). The reason for this is that diffusion at the contact between two identical minerals, whose boundaries are most often healed, is much slower than diffusion at the contact between minerals of different nature where the fluid phase boundary is more continuous [*Zubtsov et al*., 2004]. The difference is even greater if one of the minerals is a phyllosilicate, which prevents healing [*Bos and Spiers*, 2000] or activates dissolution [*Renard et al*., 2001].

4.2.2. Mass Transfer at the Mesoscale, Tectonic Layering, and Size of the Closed System

At the mesoscale, various types of structures are observed, such as tectonic stylolites, cleavages, and foliations more or less associated with veins of various sizes in the closed system. In the locked segments, tectonic stylolites are associated with tension gashes veins (Figure 3e) that have the same composition as the dissolved minerals. Even though it is not easy to evaluate exactly the size of the closed system, a mean distance of diffusive mass transfer can be evaluated, ranging from 1 to 10 cm. A schematic representation of this behavior based on diffusion-driven mass transfer is shown on the diagram of volumetric strain plotted against the size of the closed system (Figure 16a). The size of a near closed system is smaller than 1 dmr with conservation of volume ($\varepsilon_v \approx 0$).

In the volcanic rocks of the creeping segment, tectonic layering has developed at various scales from centimeter to micrometer width (Figures 6–8 and 10) leading to a foliation structure. Various markers such as rolling clasts (Figure 12i), asymmetrical folds (Figures 13f and 14f–14i), and cleavage planes at various angles to the main slipping zone (Figures 10a–10c and 12d) show that such layering developed during a shearing process more or less parallel to the present-day active right-lateral fault zones. Such layering is visible both in the present-day gouges and in the damage zones, although in the latter case successive veins have partially obliterated the initial tectonic layering (Figures 5a–15d and 14e). This layering process was thus a relatively early process. It began before the massive episodes of intense fracturing and sealing of the damage zone, but it was also reinforced by the first carbonate vein sealing episodes that prevented the dissolution of the more calcitic-silicate layers (Figures 12g and 14h). Such layering is frequently observed in deformed rocks. It can develop by a purely mechanical effect as shown experimentally by *Barnhoorn et al*. [2005], but in such a case this effect only starts to appear for very large shear strain values of more than 10. Conversely, it has been shown, also by experiment, that layering can develop at much lower strain values as a result of stress-driven chemical effects by dissolution of soluble elements and the passive concentration of insoluble elements [*Gratier et al*., 2015]. The foliation layering that develops here is clearly associated with this latter process with dissolution of quartz and feldspars and passive concentration of more insoluble minerals such as phyllosilicates and Fe and Ti oxides (Figures 8a, 8b, 8e, 9d, and 9e). It is a self-organized process: stress-driven dissolution of the soluble minerals is initiated in the areas initially richer in insoluble species as diffusive mass transfer along the interface between soluble/insoluble minerals is much faster than along the healed boundaries of the soluble minerals (see above). The passive concentration of the insoluble minerals amplifies the dissolution along layers oriented perpendicular to the maximum compressive stress. Conversely, in areas with an initial low content of insoluble minerals and clustered soluble minerals, dissolution is slower. Consequently, these areas are less deformed. They may show redeposition of the dissolved species (Figure 5e) or not (Figures 8a and 13d). They may also host the deposition of soluble carbonate minerals (Figures 12g and 14h) coming from outside (see section 4.2.3 below). In any case, they act as rigid objects that concentrate the dissolution near their boundaries, thus amplifying the differentiation and development of layered microstructures.

It is possible to estimate the mass transfer that occurred at the layering scale when comparing the mineralogical composition of the more deformed (exposed) zones relative to the zones that have been more protected from deformation. The relative mass change is: $\Delta M/M = (I_p/I_e) - 1$, $\Delta M/M$ being the relative mass change and I_p and I_e the concentrations of the whole insoluble minerals in the protected and exposed zones, respectively. As the porosity of the rock does not change to any significant degree, this mass change may be assimilated to a volume change. This relation may be used on various examples in order to evaluate the mass transfer. In Figure 8b when comparing a clast of initial rock that has been protected from deformation with zones that have been subject to greater deformation, a relative decrease in volume of -60% ($I_p = 23\%$ and $I_e = 60\%$) was found. In Figures 9d and 9e a relative decrease in volume of -40% ($I_p = 48\%$ and $I_e = 80\%$) was found. In both cases, the mobile minerals are mainly feldspars and quartz. In Figure 7d, quartz appears to behave as an insoluble mineral, which may happen if the deformation temperature is very low, with a volume change due to feldspar dissolution of about -50% ($I_p = 33\%$ and $I_e = 67\%$). An example of such behavior is modeled in Figure 16b: during shearing, the differentiation occurs with progressively increasing strain toward the center of the layer. Far away from the median axis, the rock composition does not change. As one gets closer to the median axis, each cube in the grid deforms by superposition of 10% simple shear and 10% shortening with 10% volume loss. These measurements are made at centimeter to decimeter scale, but the same layering process occurs from decimeter to micrometer scale.

When considering the wide foliated shear zone that includes both the present-day gouges and the damage zone in the early times (Figure 4), the question is to know where the soluble matter was transported. At small scale, part of this material may have reprecipitated in quartz veins (Figure 5e) but this is rarely seen. Part of the feldspars was transformed into clay minerals by metamorphic reactions (Figures 8f and 8g; see section 4.3 below). However, the major part of the soluble minerals probably left the shear zone, which was an open system (Figure 16a). Due to the size of the system, advection mass transfer associated with fluid circulation must have controlled the evacuation of mobile elements. However, the kinetics of the overall transfer was probably limited by the diffusion rate along the trapped fluid phase as discussed above.

4.2.3. Mass Transfer at Fault Scale, Fault Zone Segregation, and Size of the Closed System

As mentioned above, the layering process developed in a large shear zone that progressively evolved into the present-day gouges and damage zones. Two parallel processes controlled this evolution. The first one is fracturing and sealing of the damage zones (Figure 16a), tending to strengthen this zone because large veins of monomineralic carbonates are very difficult to deform by dissolution even if a certain amount of dissolution can be seen at their boundaries (Figures 5f, 5g, 11e, and 11f). Evidence of large veins that stop deformation is found everywhere (Figures 12d–12i). The second process is pressure solution creep that remains active in the gouge, facilitated by the concentration of insoluble minerals in a self-organized system, as described above (see section 4.2.2). The layering inherited from the development of large shear zones is amplified in the gouge. Note that the first calcite veins that probably developed at the same time in the proto-gouges and damage zones are sometimes folded in the gouge (Figures 14f–14i), probably because they were thinner than the latter veins. The thinner are the veins, the shorter are the paths of diffusive mass transfer from the intrados to the extrados of the folds and consequently the faster are the folding processes. However, this reflects a continuous change, as indicated by the folding of the foliation (Figure 13f). It must be noted that such an opposite volume change between (i) fault gouge with volume loss by mechanical wear and dissolution and (ii) damage zone with volume increase with carbonates and zeolites veins is also described in other faults such as the Nojima Fault [*Tanaka et al*., 2001].

The huge amount of carbonates that sealed the fractures in the damaged rocks, sometimes up to 90% in very large areas (Figure 4d), cannot originate from the volcanic rocks but must come from nearby limestone massifs. Consequently, an enormous mass transfer was required to accommodate this segregation process between gouge and damage zone, with a two-way fluid flux in order to (i) evacuate the dissolved species from the fault zone and (ii) bring into the fault zone the carbonates that filled the veins and some fluids that contribute to the metamorphism of the gouge (see section 4.3 below). It is likely that the flux inversions were linked to earthquakes [*Sibson*, 1990], the shear zones having been probably associated with earthquakes with postseismic inflow and interseismic outflow. Evidence of such seismic behavior can be found in historical records and the recent period [*Kondo et al*., 2005]. Earthquakes have occurred repeatedly over geological timescales, as attested by the cataclastic gouges (Figure 11d) and intense networks of carbonates veins (Figures 5a, 6d, and 14e) with euhedral mineral sealing (Figure 5c) that reflect the fast void openings commonly associated with seismic events [*Gratier et al*., 2013a]. The high Mg content (dolomite and magnesite) or Fe content (siderite) of these veins probably reflects the relatively high temperature of the fluids coming from depth after each earthquake [*Montes-Hernandez et al*., 2016]. Evidence of CO_2-rich springs seeping along the fault, as trails of CO_2 bubbles that are seen in a pond at the Ismetpasa outcrop and travertine carbonate deposition [*Temiz et al*., 2013], bears witness to the present-day regional fluid flux. Moreover, permeability in the gouges and damage zones varies over an enormous range during the seismic cycle, depending on rock type and fracture connectivity. In this context, the intriguing veins parallel to the cleavage (Figures 5a, 10a, 10b, and 14j) may be explained either by stress rotation or by hydraulic fracturing due to local overpressure [*Mittempergher et al*., 2011] or by chemically activated subcritical cracking processes [*Brantut et al*., 2013]. Hydraulic fracturing may develop parallel to the cleavage if the sum of the stress normal to the cleavage and the cleavage tensile strength is lower than the stress parallel to the cleavage and the rock tensile strength [*Gratier et al*., 2013a]. This happens mainly at depth in the context of lithological fluid pressure [*Jefferies et al*., 2006b]. However, for a crack-sealing process (Figure 5b) it is impossible to rule out other possibilities of sealing driving forces, such as the crystallization force associated with CO_2 degassing of oversaturated fluid [*Noiriel et al*., 2010], which is more likely in a near-surface context [*Gratier et al*., 2012].

It should be noted that several parallel gouges could develop, simultaneously or successively (Figure 4). Conceptually, it is the same self-organized system that the foliation development described above [*Gratier*

et al., 2015], but at regional scale (Figure 4a). This phenomenon is represented as a sketch in Figure 16c, where mineral differentiation coupled with fracture sealing controls the formation of layers with high and low friction and low and high strain localization, respectively. The transition from strong to weak behavior could possibly result from a phase transition of the rock structure from isotropic to anisotropic [*Collettini et al*., 2009]. When the shear strain is greater than a critical shear strain $\gamma > \gamma_c$, weak zones start to separate from strong zones and form alternating strong and weak zones with high and low friction values, respectively. Most of the creep deformation occurs in the weak zones (Figures 6f and 12h), whereas strong zones deform by fracturing (Figures 3a–3e and 12g).

4.3. Gouge Metamorphism and Phase Transformation

Along the North Anatolian Fault, evidence of the transformations of mica, chlorites, or feldspars to weak clay minerals is observed. Temperature and pressure vary with depth in the first few kilometers of strike slip faults as a result of tectonic forces, geothermal gradients, and fluid circulation. With typical geothermal (25°C km^{-1}) and lithostatic gradients, the temperature at 6 km depth is up to 150°C, and the lithostatic pressure is up to 150–170 MPa. Under these conditions, volcanic rocks alter and produce weak minerals, including saponite [*Andrews*, 1980*; Gíslason et al*., 1996*; Wilson*, 2004]. Such alteration is also found in other places where volcanic rocks weather, such as Iceland [*Gíslason et al*., 1996]. Plagioclases and phyllosilicates such as mica and chlorite transform into kaolinite and then to smectite (montmorillonite and saponite) as a result of hydrothermal fluid circulation along the fault [*Deer et al*., 2013]. Goethite and smectite can form as products of volcanic rock alteration, with goethite forming first, followed by smectite and a small amount of zeolites. Our XRD analyses of creeping gouges reveal the presence of these clay minerals and even ~1% of natrolite (zeolite group) (Figure 8c). This supports the idea of volcanic rock alteration into weak clay minerals. At the grain scale, the mineralogical changes occurring between protected and deformed zones can be seen in the gouge in the outcrop west of Ismetpasa (Figures 8f and 8g). For instance, in the initial (protected) state (in the undeformed volcanic clast), the plagioclase-rich clasts are composed of anorthite cores coated with labradorite and without any preferred orientation of the grains. Conversely, in the foliated gouge, all grains have lost their labradorite coating. Moreover, in addition to losing their coating, some grains lose at least 75% of their original size, with all their long axes aligned subparallel to the shear direction.

Along minor faults in serpentines, only minor changes in the chemical composition of the rock are measured, and there is no evidence of a well-developed gouge, nor is any smectite detected in the XRD data (Figure 8c). In the absence of significant tectonic or metamorphic transformations, the serpentines do not appear to be weak rocks.

It is worth noting that only part of the phyllosilicate and feldspar minerals is transformed into soft clay. Theoretically, the transformation of labradorite into smectite is driven by fast kinetics, with typical timescales of the order of one to several years [*Aharonov et al*., 1998*; Tenthorey et al*., 1998]. However, plagioclase dissolution rates are strongly dependent on composition and pH [*Gudbrandsson et al*., 2014]. Moreover, evidence of fast kinetics is most often found in the laboratory for free-face metamorphic reactions in experiments where minerals are under fluid pressure. In active deformed zones, the reactions must occur in fluid phases that are trapped under stress and, in this case, the kinetics of the reaction is controlled by the diffusive mass transfer flux along these fluid phases (see discussion in section 4.2) and the process is very slow [*Wheeler*, 2014].

The timing of these metamorphic transformations may affect creep deformation in two ways: (i) either insoluble minerals (micas, chlorites, etc.) are first passively concentrated in the gouge and then transformed into weak minerals such as smectite or kaolinite or (ii) metamorphic transformations occur first and then the weak minerals are passively concentrated in the gouge.

If metamorphic transformations occur first at a local scale with diffusion-controlled mass transfer, the transformed volume will remain small covering a maximum distance of just a few meters according to the experiments of *Ildefonse and Gabis* [1976]. The effect on the creep process will then be minimal. If such metamorphic transformations occur first but along fractures before gouge development, the gouges will also be diffuse and disconnected, again with a minimal effect on the creep process. Conversely, if metamorphic transformations occur after the passive concentration of phyllosilicates by pressure solution, and on some large feldspars that had not been dissolved previously, they will be more efficient for facilitating creep as

they occur in gouges that are already regionally connected. Transformations that occur along planar interconnected layers of the gouge greatly facilitate the amplification of the creep process [*Holdsworth et al*., 2011]. Moreover, we see plenty of evidence of early brittle and even comminution processes associated with early seismic events and associated interseismic pressure solution processes (Figures 7, 8, 11, and 12). Reducing the grain size increases the reaction rates (see below section 4.4, point 3) facilitating the localization of the pressure solution and metamorphic processes (see above section 4.2.2). This testifies of a partitioning of the deformation alternating fast brittle and slow creep processes. Such coupled brittle and ductile deformation have been described on other faults as in the Outer Hebrides Fault Zone and the Great Glen Fault in Scotland and in the Median Tectonic Line in Japan [*Stewart et al*., 2000; *Imber et al*., 2001; *Jefferies et al*., 2006a]. The formation of smectite has also been related to the infiltration of hydrothermal fluid, as reported for the Wenchuan Earthquake fault [*Chen et al*., 2013b] and the Chelungpu thrust fault [*Isaacs et al*., 2007]. In the case of the North Anatolian Fault, these transformations could have occurred relatively early in proto-gouges that were later included in vein networks of the damage zones (Figures 5f and 5g). This is consistent with the observations of high fluid fluxes associated with the postseismic processes described above. Such large fluid transfers along the gouge have two effects: the transformation of relatively rigid minerals into weak minerals that soften the gouge and the extensive deposition of soluble carbonate minerals in the damage zone, which strengthen this zone.

4.4. Aseismic Creep Mechanisms

First, it should be noted that both creeping segments and currently locked fault segments actually show considerable geological evidence of creep (Figures 3–14). Creep is still active along the Izmit and Ismetpasa segments, since the 1999 Izmit and 1944 Dücze earthquakes, while some of it is fossil and was associated with afterslip and postseismic creep following older major past earthquakes. This section discusses the four types of mechanism of creep in present-day and past creeping and locked segments.

Numerous occurrences of stylolites and cleavage, associated with veins to a varying extent, and dissolution features at grain scale (Figures 3–14) bear witness to an efficient process of pressure solution ductile deformation. The pressure solution viscous creep law, derived from experiments [*Rutter*, 1976*; Bos and Spiers*, 2000; *Gratier et al*., 2011], states that the strain rate is inversely proportional to the cube of the diffusive mass transfer distance along the fluid phase that is trapped under stress. Consequently, it is possible to evaluate the relation between the mass transfer distance inferred from our observations and the displacement rate and width of the deforming zone.

1. In the currently locked zones, pressure solution is associated with mass transfer distances of 1 to 10 cm. However, the highly stylolitic zones with 1 cm transfer are rather narrow (1 m width at most), and those with 10 cm transfer distance are found only over a small width of the total damage zone (10 m at most). At 5 km depth, for calcite [*Gratier et al*., 2011], a 1 cm mass transfer distance in a 1 m shear zone could potentially lead to a strain rate of 2.6×10^{-15} s^{-1}, which corresponds to a displacement rate of 0.15 μm/yr, and for a 10 cm mass transfer distance in a 10 m wide shear zone the displacement rate would be 0.0015 μm/yr. Clearly, it is not possible to measure and record such very low displacement rates with classical surface geodetic measurements. So even if creep is active, the zone still appears locked.
2. In the wide shear zones preceding gouge development, pressure solution cleavage was associated with foliation development. In this case, if the diffusive mass transfer distance for feldspar and quartz dissolution was of the order of the foliation width (1 mm), a shear zone of 10 to 50 m width could potentially have accommodated a displacement rate of 10 mm/yr [*Gratier et al*., 2011].
3. An increase in shear leads to the distortion of cleavage surfaces from 45° at the initial step to near 0° after a large shear displacement [*Ramsay*, 1967], as observed in our data (Figure 10a). When cleavages are distorted down to low angles with respect to the gouge, the creep mechanism changes to a grain boundary sliding process accommodated by a pressure solution diffusion mechanism. However, this mechanism of grain boundary sliding can only develop if the gouge contains a significant amount of soluble species as in some foliated gouges of the creeping segment (Figures 8e, 12h, and 14g). This mechanism is geometrically analogous to the superplasticity process described by *Ashby and Verrall* [1973]. It can accommodate almost infinite shear strain values, and the strain rate is inversely proportional to the cube of the grain size. It was suggested that superplasticity occurs at high temperatures in dry rocks either in the bulk grain mineral or at their boundaries [*Boullier and Gueguen*, 1975]. It was even suggested that thin films of

nanogranular fault rock could allow superplasticity to accommodate unstable seismic fault slip [*Verbene et al*., 2014]. Here at 5 km depth in wet rocks, assuming a mean value of 10 mm/yr and a gouge width of 50 cm, and due to the inverse relation between strain rate and cube of the grain size, the maximum grain size for feldspars and quartz would range from 200 to 400 μm, respectively [*Gratier et al*., 2011]. If the gouge were thinner (10 cm), the required grain sizes would be smaller, ranging from 100 to 250 μm. When considering the thin sections, it is clear that the easily deformed part (weak foliation layers, Figures 8e, 12h, and 14g) was made up of a material with a much smaller grain size than required, so active pressure solution creep is a possible mechanism. In the part that does not deform easily (strong granular or calcitic-silicate layers that break or are disrupted), the grain size is close to or greater than these maximum values required to develop grain boundary sliding (Figures 8e and 13d). This shows that pressure solution is a major mechanism governing aseismic sliding in wet rocks at low temperature in the presence of small-size soluble minerals. Diffusion occurs along a fluid water phase trapped at the boundary of the minerals and is activated by the presence of insoluble species such as phyllosilicate minerals.

4. Finally, in some of the gouge with low soluble species content where most of the soluble species (quartz and feldspars) have been dissolved or can no longer be dissolved because they are too dispersed, the gouge contains localized layers of phyllosilicate and clays minerals. The phyllosilicates are most often well reoriented, whereas the clays (smectite) show no preferred mineral orientation (Figures 5f and 6f). In this case, the friction of the gouge depends on the friction of individual minerals and on the geometry of their assemblage [*Moore et al*., 1997*; Carpenter et al*., 2011*; Lockner et al*., 2011*; Sone et al*., 2012*; Carpenter et al*., 2016] or on a combined frictional and viscous flow behavior [*Bos and Spiers*, 2002]. In the North Anatolian Fault example, the friction becomes very low because of the passive concentration of phyllosilicates that progressively transform into smectites, which appear in layering at various spatial scales in the range 10^{-5} m to 10^{-2} m.

From a general point of view, and to summarize the discussion, the contrast in change in limestone and volcanic rock deformation is shown in Figure 16d: (i) limestone units deform mainly by seismic displacement with only very minor postseismic aseismic displacement, and this behavior is stable with time, and (ii) volcanic rock units deform by both seismic and aseismic displacements associated with a chemical change in the rocks during geological times involving mass transfer in and out of the fault zone. This leads to gouge softening and damage zone strengthening and a change from diffuse to localized seismic-aseismic zones. Such mineral transformation can lead to permanent or transient aseismic sliding, as observed in other creeping faults that contain similar material such as the San Andreas Fault in California [*Lockner et al*., 2011; *Richard et al*., 2014] and the Long Valley Fault [*Thomas et al*., 2014a, 2014b]. It might be worth to note that the clay-rich fault gouges generally have lower permeabilities than clay-free gouges, which may also affect the runaway process of an earthquake, e.g., by thermal or thermochemical pressurization [*Wibberley and Shimamoto*, 2003; *Chen et al*., 2013a].

5. Conclusions

Based on the observations of fault zone outcrops along the North Anatolian Fault, the main findings of the present study can be summarized as follows:

1. There is a clear correlation between shallow creep and near-surface fault gouge composition. The locked fault segments consisting of massive limestone without any clay gouge are deformed mainly seismically. The creeping segments are located in volcanic units that show decimeter-thick clay gouges with high phyllosilicate and clay minerals content; they accommodate displacement along fault both by seismic and aseismic slip.
2. The clay gouges in the creeping segments result from a progressive change of the initial volcanic rocks during their deformation. A large damage zone is initially formed by shearing during the first stage of displacement, leading to layering development obliquely then subparallel to the fault that accommodates part of the aseismic displacement by pressure solution creep. Soluble minerals, mainly quartz and feldspars, are dissolved and evacuated for the most part by fluid advection out of the deforming zone during interseismic periods, leading to passive concentration of phyllosilicates in the gouges.
3. The damage zones, in parallel, are fractured by seismic events, and numerous fracture networks are sealed by carbonate minerals coming from outside during postseismic inflow. This fluid inflow also induces

metamorphic transformations of the passively concentrated phyllosilicates, and of some large feldspars not previously dissolved, producing low-friction clay minerals such as kaolinite and smectite. As a result, these mineralogical and structural transformations weaken the gouges and strengthen the damage zones, leading to a change from diffuse to localized seismic-aseismic zones.

4. The mechanisms of aseismic creep are a combination of pressure solution creep and friction sliding. These mechanisms evolve with time. Pressure solution creep is the driving force in early shear zones with the development of cleavage and layering. It is subsequently superseded by grain boundary sliding in the gouges, which still contain soluble minerals. In places where the soluble species have been completely dissolved or can no longer be dissolved because of their dispersion, then low-friction minerals control aseismic sliding.

Acknowledgments
This project was funded by the European Union's, Seventh Framework Programme for research technological development and demonstration under grant agreement 316889 (ITN FlowTrans) and by the CNRS-INSU (programs Syster and ALEAS). This work has been supported by a grant from Labex OSUG@2020 (Investissements d'avenir - ANR10 LABX56) and by the Frinatek grant 250661 (HADES) from the Norwegian Research Council. The authors would like to thank N. Findling, V. Magnin, and V. Batanova for technical support with measurement equipment at ISTerre, A.-M. Boullier for her help in microstructural analyses, and B. Rousset and F. Aben for their help on the field. The microstructural and mineralogical data in the present study can be requested from the corresponding author. We thank R.E. Holdsworth and three anonymous reviewers for their comments that significantly improved the manuscript.

References

Akbayram, K., C. C. Sorlien, and A. L. Okay (2016), Evidence for a minimum 52 ± km of total offset along the northern branch of the North Anatolian Fault in northwest Turkey, *Tectonophysics*, *668–669*, 35–41, doi:10.13140/RG.2.1.4160.8729.

Adiyaman, Ö., J. Chorowicz, O. N. Arnaud, M. N. Gündogdu, and A. Gourgaud (2001), Late Cenozoic tectonics and volcanism along the North Anatolian Fault: New structural and geochemical data, *Tectonophysics*, *338*(2), 135–165, doi:10.1016/S0040-1951(01)00131-7.

Aharonov, E., E. Tenthorey, and C. H. Scholz (1998), Precipitation sealing and diagenesis: 2. Theoretical analysis, *J. Geophys. Res.*, *103*(B10), 23,969–23,981, doi:10.1029/98JB02230.

Akbaş, B., et al. (2016), Turkey geology map general directorate of mineral research and exploration publications, Ankara Turkey.

Ambraseys, N. N. (1970), Some characteristic features of the Anatolian fault zone, *Tectonophysics*, *9*(2–3), 143–165, doi:10.1016/0040-1951(70)90014-4.

Andrews, A. J. (1980), Saponite and celadonite in layer 2 basalts, DSDP Leg 37, *Contrib. to Mineral. Petrol.*, *73*(4), 323–340, doi:10.1007/BF00376627.

Armijo, R., B. Meyer, A. Hubert, and A. Barka (1999), Westward propagation of the North Anatolian fault into the northern Aegean: Timing and kinematics, *Geology*, *27*(3), 267, doi:10.1130/0091-7613(1999)027<0267:WPOTNA>2.3.CO;2.

Armijo, R., B. Meyer, A. Hubert, and A. Barka (2000), Westward propagation of North Anatolian fault into the northern Aegean: Timing and kinematics—Comment and reply, *Geology*, *28*(2), 188, doi:10.1130/0091-7613(2000)28<188:WPONAF>2.0.CO;2.

Armijo, R., et al. (2005), Submarine fault scarps in the Sea of Marmara pull-apart (North Anatolian Fault): Implications for seismic hazard in Istanbul, *Geochem. Geophys. Geosyst.*, *6*, Q06009, doi:10.1029/2004GC000896.

Ashby, M., and R. Verrall (1973), Diffusion-accommodated flow and superplasticity, *Acta Metall.*, *11*(2), 149–163.

Atkinson, B. K. (1984), Subcritical crack growth in geological materials, *J. Geophys. Res.*, *89*(B6), 4077–4114, doi:10.1029/JB089iB06p04077.

Barbot, S., N. Lapusta, and J.-P. Avouac (2012), Under the hood of the earthquake machine: Toward predictive modeling of the seismic cycle, *Science*, *336*(6082), 707–710, doi:10.1126/science.1218796.

Barka, A. (1992), The North Anatolian fault zone, Ann, *Tectonicae*, *6*(Suppl), 164–195.

Barka, A., and R. Reilinger (1997), Active tectonics of the Eastern Mediterranean region: Deduced from GPS, neotectonic and seismic data, *Ann. di Geofis.*, *40*, 587–6190, doi:10.1111/j.1365-2486.2011.02460.x.

Barnhoorn, A., M. Bystricky, K. Kunze, L. Burlini, and J.-P. Burg (2005), Strain localisation in bimineralic rocks: Experimental deformation of synthetic calcite-anhydrite aggregates, *Earth Planet. Sci. Lett.*, *240*(3–4), 748–763, doi:10.1016/j.epsl.2005.09.014.

Bilham, R., et al. (2016), Surface creep on the North Anatolian Fault at Ismetpasa, Turkey, 1944–2016, *J. Geophys. Res. Solid Earth*, *121*, 7409–7431, doi:10.1002/2016JB013394.

Bullock, R. J., N. de Paola, and R. E. Holdsworth (2015), An experiemntal investigation into the role of phyllosilicates content on earthquake propagation during seismic slip in carbonate faults, *J. Geophys. Res. Solid Earth*, *120*, 3187–3207, doi:10.1002/2015JB011914.

Beroza, G. C., and S. Ide (2011), Slow earthquakes and nonvolcanic tremor, *Annu. Rev. Earth Planet. Sci.*, *39*(1), 271–296, doi:10.1146/annurev-earth-040809-152531.

Bos, B., and C. J. Spiers (2000), Effect of phyllosilicates on fluid-assisted healing of gouge-bearing faults, *Earth Planet. Sci. Lett.*, *184*(1), 199–210, doi:10.1016/S0012-821X(00)00304-6.

Bos, B. and C. J. Spiers (2002), Frictional-viscous flow of phyllosilicate-bearing fault rock: Microphysical model and implications for crustal strength profiles, *J. Geophys. Res.*, *107*(B2), 2028, doi:10.1029/2001JB000301.

Bouchon, M., H. Karabulut, M. Aktar, S. Ozalaybey, J. Schmittbuhl, and M.-P. Bouin (2011), Extended nucleation of the 1999 M_w 7.6 Izmit earthquake, *Science*, *331*(6019), 877–880, doi:10.1126/science.1197341.

Bouchon, M., V. Durand, D. Marsan, H. Karabulut, and J. Schmittbuhl (2013), The long precursory phase of most large interplate earthquakes, *Nat. Geosci.*, *6*(4), 299–302, doi:10.1038/ngeo1770.

Boullier, A.-M., and Y. Gueguen (1975), SP-Mylonites: Origin of some mylonites by superplastic flow, *Contrib. to Mineral. Petrol.*, *50*(2), 93–104, doi:10.1007/BF00373329.

Brantut, N., M. Heap, P. Meredith, and P. Baud (2013), Time-dependent cracking and brittle creep in crustal rocks: A review, *J. Struct. Geol.*, *52*, 17–43, doi:10.1016/j.jsg.2013.03.007.

Çakir, Z., J.-B. de Chabalier, R. Armijo, B. Meyer, A. Barka, and G. Peltzer (2003), Coseismic and early post-seismic slip associated with the 1999 Izmit earthquake (Turkey), from SAR interferometry and tectonic field observations, *Geophys. J. Int.*, *155*(1), 93–110, doi:10.1046/j.1365-246X.2003.02001.x.

Çakir, Z., A. M. Akoglu, S. Belabbes, S. Ergintav, and M. Meghraoui (2005), Creeping along the Ismetpasa section of the North Anatolian fault (Western Turkey): Rate and extent from InSAR, *Earth Planet. Sci. Lett.*, *238*(1–2), 225–234, doi:10.1016/j.epsl.2005.06.044.

Çakir, Z., S. Ergintav, H. Ozener, U. Dogan, A. M. Akoglu, M. Meghraoui, and R. Reilinger (2012), Onset of aseismic creep on major strike-slip faults, *Geology*, *40*(12), 1115–1118, doi:10.1130/G33522.1.

Carpenter, B. M., C. Marone, and D. M. Saffer (2011), Weakness of the San Andreas Fault revealed by samples from the active fault zone, *Nat. Geosci.*, *4*(4), 251–254, doi:10.1038/ngeo1089.

Carpenter, B. M., M. J. Ikari, and C. Marone (2016), Laboratory observations of time-dependent frictional strengthening and stress relaxation in natural and synthetic fault gouges, *J. Geophys. Res. Solid Earth*, *121*, 1183–1201, doi:10.1002/2015JB012136.

Cetin, E., Z. Çakir, M. Meghraoui, S. Ergintav, and A. M. Akoglu (2014), Extent and distribution of aseismic slip on the Ismetpasa segment of the North Anatolian Fault (Turkey) from Persistent Scatterer InSAR, *Geochem. Geophys. Geosyst.*, *15*, 2883–2894, doi:10.1002/2014GC005307.

Chen, J., X. Yang, Q. Duan, T. Shimamoto, and C. J. Spiers (2013a), Importance of thermochemical pressurization in the dynamic weakening of the Longmenshan Fault during the 2008 Wenchuan earthquake: Inferences from experiments and modeling, *J. Geophys. Res. Solid Earth*, *118*, 4145–4169, doi:10.1002/jgrb.50260.

Chen, J., X. Yang, S. Ma, and C. J. Spiers (2013b), Mass removal and clay mineral dehydration/rehydration in carbonate-rich surface exposures of the 2008 Wenchuan Earthquake fault: Geochemical evidence and implications for fault zone evolution and coseismic slip, *J. Geophys. Res. Solid Earth*, *118*, 474–496, doi:10.1002/jgrb.50089.

Chester, F., J. Chester, D. Kirschner, S. Schulz, and J. Evans (2004), Structure of large-displacement, strike-slip fault zones in the brittle continental crust, *Rheol. Deform. Lithosph. Cont. Margins*, *1*, 223–260.

Collettini, C., A. Niemeijer, C. Viti, and C. Marone (2009), Fault zone fabric and fault weakness, *Nature*, *462*(7275), 907–910, doi:10.1038/nature08585.

Collettini, C., C. Viti, T. Tesei, and S. Mollo (2013), Thermal decomposition along natural carbonate faults during earthquakes, *Geology*, *41*, 927–930.

Deer, W. A., R. A. Howie, and J. Zussman (2013), *An Introduction to the Rock-Forming Minerals*, 488 pp., Mineralogical Society of Great Britain & Ireland ed, Twickenham, U. K.

de Michele, M., D. Raucoules, F. Rolandone, P. Briole, J. Salichon, A. Lemoine, and H. Aochi (2011), Spatiotemporal evolution of surface creep in the Parkfield region of the San Andreas Fault (1993–2004) from synthetic aperture radar, *Earth Planet. Sci. Lett.*, *308*(1–2), 141–150, doi:10.1016/j.epsl.2011.05.049.

den Hartog, S. A. M., A. R. Niemeijer, and C. J. Spiers (2013), Friction on subduction megathrust faults: Beyond the illite–muscovite transition, *Earth Planet. Scie. Lett.*, *373*, 8–19, doi:10.1016/j.epsl.2013.04.036.

Doebelin, N., and R. Kleeberg (2015), Profex: A graphical user interface for the Rietveld refinement program BGMN, *J. Appl. Crystallogr.*, *48*(5), 1573–1580, doi:10.1107/S1600576715014685.

Dor, O., C. Yildirim, T. K. Rockwell, Y. Ben-Zion, O. Emre, M. Sisk, and T. Y. Duman (2008), Geological and geomorphologic asymmetry across the rupture zones of the 1943 and 1944 earthquakes on the North Anatolian Fault: Possible signals for preferred earthquake propagation direction, *Geophys. J. Int.*, *173*(2), 483–504, doi:10.1111/j.1365-246X.2008.03709.x.

Ellero, A., G. Ottria, M. Marroni, L. Pandolfi, and M. C. Göncüoğlu (2015), Analysis of the North Anatolian Shear Zone in Central Pontides (northern Turkey): Insight for geometries and kinematics of deformation structures in a transpressional zone, *J. Struct. Geol.*, *72*, 124–141, doi:10.1016/j.jsg.2014.12.003.

Elliott, D. (1973), Diffusion flow laws in metamorphic rocks, *Geol. Soc. Am. Bull.*, *84*(8), 2645, doi:10.1130/0016-7606.

Emre, Ö., T. Y. Duman, S. Özalp, H. Elmacı, Ş. Olgun, and F. Şaroğlu (2013), Active fault map of Turkey with an explanatory text. 1:1,250,000 scale, General Directorate of Mineral Research and Exploration (MTA), Ankara-Turkey.

Fattahi, H., and F. Amelung (2016), InSAR observations of strain accumulation and fault creep along the Chaman Fault system, Pakistan and Afghanistan, *Geophys. Res. Lett.*, *43*, 8399–8406, doi:10.1002/2016GL07121.

Flerit, F., R. Armijo, G. C. P. King, B. Meyer, and A. Barka (2003), Slip partitioning in the Sea of Marmara pull-apart determined from GPS velocity vectors, *Geophys. J. Int.*, *154*(1), 1–7, doi:10.1046/j.1365-246X.2003.01899.x.

Fondriest, M., S. A. Smith, T. Candela, S. B. Nielsen, K. Mair, and G. Di Toro (2013), Mirror-like faults and power dissipation during earthquakes, *Geology*, *41*(11), 1175–1178.

Gasperini, L., A. Polonia, M. N. Çağatay, G. Bortoluzzi, and V. Ferrante (2011), Geological slip rates along the North Anatolian Fault in the Marmara region, *Tectonics*, *30*, TC6001, doi:10.1029/2011TC002906.

Gíslason, S. R., S. Arnórsson, and H. Ármannsson (1996), Chemical weathering of basalt in Southwest Iceland: Effects of runoff, age of rocks and vegetative/glacial cover, *Am. J. Sci.*, *296*(8), 837–907, doi:10.2475/ajs.296.8.837.

Göncüoglu, M. C. (2010), *Introduction to the Geology of Turkey: Geodynamic Evolution of the pre-Alpine and Alpine Terranes*, *Monogr. Ser.*, 66 pp., MTA, Ankara.

Grall, C., P. Henry, Y. Thomas, G. K. Westbrook, M. N. Çağatay, B. Marsset, H. Saritas, G. Çifçi, and L. Géli (2013), Slip rate estimation along the western segment of the Main Marmara Fault over the last 405–490 ka by correlating mass transport deposits, *Tectonics*, *32*, 1587–1601, doi:10.1002/2012TC003255.

Gratier, J.-P., J. Richard, F. Renard, S. Mittempergher, M.-L. Doan, G. Di Toro, J. Hadizadeh, and A.-M. Boullier (2011), Aseismic sliding of active faults by pressure solution creep: Evidence from the San Andreas Fault Observatory at Depth, *Geology*, *39*(12), 1131–1134, doi:10.1130/G32073.1.

Gratier, J.-P., E. Frery, P. Deschamps, A. Royne, F. Renard, D. K. Dysthe, N. Ellouz-Zimmerman, and B. Hamelin (2012), How travertine veins grow from top to bottom and lift the rocks above them: The effect of crystallization force, *Geology*, *40*(11), 1015–1018, doi:10.1130/G33286.1.

Gratier, J.-P., D. K. Dysthe, and F. Renard (2013a), The role of pressure solution creep in the ductility of the Earth's upper crust, *Advance in Geophysics*, *54*, 47–171.

Gratier, J.-P., F. Thouvenot, L. Jenatton, A. Tourette, M.-L. Doan, and F. Renard (2013b), Geological control of the partitioning between seismic and aseismic sliding behaviours in active faults: Evidence from the Western Alps, France, *Tectonophysics*, *600*, 226–242, doi:10.1016/j.tecto.2013.02.013.

Gratier, J.-P., C. Noiriel, and F. Renard (2015), Experimental evidence for rock layering development by pressure solution, *Geology*, *43*(10), 871–874, doi:10.1130/G36713.1.

Gudbrandsson, S., D. Wolff-Boenisch, S. R. Gislason, and E. H. Oelkers (2014), Experimental determination of plagioclase dissolution rates as a function of its composition and pH at 22°C, *Geochim. Cosmochim. Acta*, *139*, 154–172, doi:10.1016/j.gca.2014.04.028.

Hadizadeh, J., S. Mittempergher, J.-P. Gratier, F. Renard, G. Di Toro, J. Richard, and H. A. Babaie (2012), A microstructural study of fault rocks from the SAFOD: Implications for the deformation mechanisms and strength of the creeping segment of the San Andreas Fault, *J. Struct. Geol.*, *42*, 246–260, doi:10.1016/j.jsg.2012.04.011.

Hearn, E. H., S. McClusky, S. Ergintav, and R. E. Reilinger (2009), Izmit earthquake postseismic deformation and dynamics of the North Anatolian Fault Zone, *J. Geophys. Res.*, *114*, B08405, doi:10.1029/2008JB006026.

Herece, E. I., and E. Akay (2003), *Atlas of North Anatolian Fault*, General Directorate of Mineral Research and Exploration (MTA), 14 pp., Ankara-Turkey.

Holdsworth, R. E., E. W. E. van Diggelen, C. J. Spiers, J. H. P. de Bresser, R. J. Walker, and L. Bowen (2011), Fault rocks from the SAFOD core samples: Implications for weakening at shallow depths along the San Andreas Fault, California, *J. Struct. Geol.*, *33*(2), 132–144, doi:10.1016/j.jsg.2010.11.010.

Hubert-Ferrari, A. (2002), Morphology, displacement, and slip rates along the North Anatolian Fault, Turkey, *J. Geophys. Res.*, *107*(B10), 2235, doi:10.1029/2001JB000393.

Hussain, E., T. J. Wright, R. J. Walters, D. Bekaert, A. Hooper, and G. A. Houseman (2016a), Geodetic observations of postseismic creep in the decade after the 1999 Izmit earthquake, Turkey: Implications for a shallow slip deficit, *J. Geophys. Res. Solid Earth*, *121*, 2980–3001, doi:10.1002/2015JB012737.

Hussain, E., A. Hooper, T. J. Wright, R. J. Walters, and D. P. S. Bekaert (2016b), Interseismic strain accumulation across the central North Anatolian Fault from iteratively unwrapped InSAR measurements, *J. Geophys. Res. Solid Earth*, *121*, 9000–9019, doi:10.1002/2016JB013108.

Ildefonse, J., and V. Gabis (1976), Experimental study of silica diffusion during metasomatic reactions in the presence of water at 550 C and 1000 bars, *Geochim. Cosmochim. Acta*, *40*(3), 292–303, doi:10.1016/0016-7037(76)90206-4.

Imber, J., R. E. Holdsworth, C. A. Butler, and R. A. Strachan (2001), A reppraisal of the Sibson-Scholz fault model: The nature of the frictional to viscous (brittle-ductile) transition along a long-lived crustal-scale fault, Outer Hebrides, Scotland, *Tectonics*, *20*, 601–624, doi:10.1029/2000TC001250.

Isaacs, A. J., J. P. Evans, S.-R. Song, and P. T. Kolesar (2007), Structural, mineralogical, and geochemical characterization of the Chelungpu thrust fault, Taiwan, *Terr. Atmos. Ocean. Sci.*, *18*(2), 183–221.

Janssen, C., G. W. Michel, M. Bau, V. Lüders, and K. Mühle (1997), The North Anatolian Fault Zone and the role of fluids in seismogenic deformation, *J. Geol.*, *105*(3), 387–404, doi:10.1086/515934.

Jefferies, S. P., R. E. Holdsworth, C. A. J. Wibberley, T. Shimamoto, C. J. Spiers, A. R. Niemeijer, and G. E. Lloyd (2006a), The nature and importance of phyllonite development in crustal-scale fault cores: An example from the Median Tectonic Line, Japan, *Journal of Structural Geology*, *28*, 220–235.

Jefferies, S. P., R. E. Holdsworth, T. Shimamoto, H. Takagi, G. E. Lloyd, and C. J. Spiers (2006b), Origin and mechanical significance of foliated cataclastic rocks in the cores of crustal-scale faults: Examples from the Median Tectonic Line, Japan, *J. Geophys. Res.*, *111*, B12303, doi:10.1029/2005JB004205.

Jolivet, R., C. Lasserre, M.-P. Doin, S. Guillaso, G. Peltzer, R. Dailu, J. Sun, Z.-K. Shen, and X. Xu (2012), Shallow creep on the Haiyuan fault (Gansu, China) revealed by SAR interferometry, *J. Geophys. Res.*, *117*, B06401, doi:10.1029/2011JB008732.

Jolivet, R., C. Lasserre, M.-P. Doin, G. Peltzer, J.-P. Avouac, J. Sun, and R. Dailu (2013), Spatio-temporal evolution of aseismic slip along the Haiyuan fault, China: Implications for fault frictional properties, *Earth Planet. Sci. Lett.*, *377-378*, 23–33, doi:10.1016/j.epsl.2013.07.020.

Jolivet, R., T. Candela, C. Lasserre, F. Renard, Y. Klinger, and M.-P. Doin (2015), The burst-like behavior of aseismic slip on a rough fault: The creeping section of the Haiyuan Fault, China, *Bull. Seismol. Soc. Am.*, *105*(1), 480–488, doi:10.1785/0120140237.

Jouanne, F., F. A. Audemard, C. Beck, A. Van Welden, R. Ollarves, and C. Reinoza (2011), Present-day deformation along the El Pilar Fault in eastern Venezuela: Evidence of creep along a major transform boundary, *J. Geodyn.*, *51*(5), 398–410, doi:10.1016/j.jog.2010.11.003.

Kaneko, Y., Y. Fialko, D. T. Sandwell, X. Tong, and M. Furuya (2013), Interseismic deformation and creep along the central section of the North Anatolian Fault (Turkey): InSAR observations and implications for rate-and-state friction properties, *J. Geophys. Res. Solid Earth*, *118*, 316–331, doi:10.1029/2012JB009661.

Kondo, H., Y. Awata, O. Emre, A. Dogan, S. Ozalp, F. Tokay, C. Ildirim, T. Yoshioka, and K. Okuumura (2005), Slip distribution, fault geometry and fault segmentation of the 1944 Bolu-Gerede earthquake rupture, North Anatolian Fault, Turkey, *Bull. Seism. Soc. Am.*, *95*(4), 1234–1249.

Kondo, H., V. Özaksoy, and C. Yıldirim (2010), Slip history of the 1944 Bolu-Gerede earthquake rupture along the North Anatolian fault system: Implications for recurrence behavior of multisegment earthquakes, *J. Geophys. Res.*, *115*, B04316, doi:10.1029/2009JB006413.

Kozaci, Ö., J. F. Dolan, R. Finkel, and R. Hartleb (2007), Late Holocene slip rate for the North Anatolian fault, Turkey, from cosmogenic 36Cl geochronology: Implications for the constancy of fault loading and strain release rates, *Geology*, *35*(10), 867, doi:10.1130/G23187A.1.

Kozacı, Ö., J. F. Dolan, and R. C. Finkel (2009), A late Holocene slip rate for the central North Anatolian fault, at Tahtaköprü, Turkey, from cosmogenic ^{10}Be geochronology: Implications for fault loading and strain release rates, *J. Geophys. Res.*, *114*, B01405, doi:10.1029/2008JB005760.

Lanari, P., O. Vidal, V. De Andrade, B. Dubacq, E. Lewin, E. G. Grosch, and S. Schwartz (2014), Computers & Geosciences XMapTools: A MATLAB©-based program for electron microprobe X-ray image processing and geothermobarometry, *Comput. Geosci.*, *62*, 227–240, doi:10.1016/j.cageo.2013.08.010.

Le Pichon, X. (2003), The North Anatolian Fault in the Sea of Marmara, *J. Geophys. Res.*, *108*(B4), 2179, doi:10.1029/2002JB001862.

Lockner, D. A., C. Morrow, D. Moore, and S. Hickman (2011), Low strength of deep San Andreas fault gouge from SAFOD core, *Nature*, *472*(7341), 82–85, doi:10.1038/nature09927.

Marone, C. (1998), Laboratory-derived friction laws and their application to seismic faulting, *Annu. Rev. Earth Planet. Sci.*, *26*(1), 643–696, doi:10.1146/annurev.earth.26.1.643.

McClusky, S., et al. (2000), Global Positioning System constraints on plate kinematics and dynamics in the eastern Mediterranean and Caucasus, *J. Geophys. Res.*, *105*(B3), 5695–5719, doi:10.1029/1999JB900351.

Meade, B. J., B. H. Hager, S. C. McClusky, R. E. Reilinger, S. Ergintav, O. Lenk, A. Barka, and H. Özener (2002), Estimates of seismic potential in the Marmara Sea region from block models of secular deformation constrained by Global Positioning System measurements, *Bull. Seismol. Soc. Am.*, *92*(1), 208–215, doi:10.1785/0120000837.

Meghraoui, M., M. E. Aksoy, H. S. Akyüz, M. Ferry, A. Dikbaş, and E. Altunel (2012), Paleoseismology of the North Anatolian Fault at Güzelköy (Ganos segment, Turkey): Size and recurrence time of earthquake ruptures west of the Sea of Marmara, *Geochem., Geophys. Geosyst.*, *13*, Q04005, doi:10.1029/2011GC003960.

Mittempergher, S., G. Di Toro, J.-P. Gratier, J. Hadizadeh, S. A. F. Smith, and R. Spiess (2011), Evidence of transient increases of fluid pressure in SAFOD phase III cores, *Geophys. Res. Lett.*, *38*, L03301, doi:10.1029/2010GL046129.

Montes-Hernandez, G., N. Findling, and F. Renard (2016), Dissolution-precipitation reactions controlling fast formation of dolomite under hydrothermal conditions, *Appl. Geochem.*, *73*, 169–177, doi:10.1016/j.apgeochem.2016.08.011.

Moore, D. E., and M. J. Rymer (2007), Talc-bearing serpentinite and the creeping section of the San Andreas fault, *Nature*, *448*(7155), 795–797, doi:10.1038/nature06064.

Moore, D. E., D. A. Lockner, S. Ma, R. Summers, and J. D. Byerlee (1997), Strengths of serpentinite gouges at elevated temperatures, *J. Geophys. Res.*, *102*(B7), 14,787–14,801, doi:10.1029/97JB00995.

Noiriel, C., F. Renard, M.-L. Doan, and J.-P. Gratier (2010), Intense fracturing and fracture sealing induced by mineral growth in porous rocks, *Chem. Geol.*, *269*(3–4), 197–209, doi:10.1016/j.chemgeo.2009.09.018.

Ozakin, Y., Y. BenZion, M. Aktar, H. Karabulut, and Z. Peng (2012), Velocity contrast across the 1944 rupture zone of the North Anatolian fault east of Ismetpasa from analysis of teleseismic arrivals, *Geophys. Res. Lett.*, *39*, L08307, doi:10.1029/2012GL051426.

Peng, Z., and J. Gomberg (2010), An integrated perspective of the continuum between earthquakes and slow-slip phenomena, *Nat. Geosci.*, *3*(9), 599–607, doi:10.1038/ngeo940.

Perfettini, H., and J.-P. Avouac (2004), Postseismic relaxation driven by brittle creep: A possible mechanism to reconcile geodetic measurements and the decay rate of aftershocks, application to the Chi-Chi earthquake, Taiwan, *J. Geophys. Res.*, *109*, B02304, doi:10.1029/2003JB002488.

Pousse Beltram, L., E. Pathier, F. Jouhanne, R. Vassallo, C. Reinoza, F. Audemard, M.-P. Doin, and M. Volat (2016), Spatial and temporal variations in creep rate along the El Pilar fault at the Caribbean-South American plate boundary (Venezuela), from InSAR, *J. Geophys. Res., Solid Earth*, *121*, 8276–8296, doi:10.1002/2016JB013121.

Ramsay, J. G. (1967), *Folding and Fracturing of Rocks*, 588 pp., McGraw-Hill, New York.

Reilinger, R., et al. (2006), GPS constraints on continental deformation in the Africa-Arabia-Eurasia continental collision zone and implications for the dynamics of plate interactions, *J. Geophys. Res.*, *111*, B05411, doi:10.1029/2005JB004051.

Reilinger, R., S. McClusky, D. Paradissis, S. Ergintav, and P. Vernant (2010), Geodetic constraints on the tectonic evolution of the Aegean region and strain accumulation along the Hellenic subduction zone, *Tectonophysics*, *488*(1–4), 22–30, doi:10.1016/j.tecto.2009.05.027.

Renard, F., D. K. Dysthe, J. Feder, K. Bjørlykke, and B. Jamtveit (2001), Enhanced pressure solution creep rates induced by clay particles: Experimental evidence in salt aggregates, *Geophys. Res. Lett.*, *28*(7), 1295–1298, doi:10.1029/2000GL012394.

Richard, J., J.-P. Gratier, M.-L. Doan, A.-M. Boullier, and F. Renard (2014), Rock and mineral transformations in a fault zone leading to permanent creep: Interactions between brittle and viscous mechanisms in the San Andreas Fault, *J. Geophys. Res. Solid Earth*, *119*, 8132–8153, doi:10.1002/2014JB011489.

Rousset, B., R. Jolivet, M. Simons, C. Lasserre, B. Riel, P. Milillo, Z. Çakir, and F. Renard (2016), An aseismic slip transient on the North Anatolian Fault, *Geophys. Res. Lett.*, *43*, 3254–3262, doi:10.1002/2016GL068250.

Rowe, C. D., A. Fagereng, J. A. Miller, and B. Mapani (2012), Signature of coseismic decarbonation in dolomitic fault rocks of the Naukluft Thrust, Namibia, *Earth and Planet. Sci. Lett.*, *333–334*, 200–210.

Rutter, E. H. (1976), The kinetics of rock deformation by pressure solution, *Philos. Trans. R. Soc. London, Ser. A*, *283*(1312), 203–219, doi:10.1098/rsta.1976.0079.

Samuelson, J., and C. J. Spiers (2012), Fault friction and slip stability not affected by CO_2 storage: Evidence from short-term laboratory experiments on North Sea reservoir sandstones and caprocks, *Int. J. Greenh. Gas Control*, *11*(SUPPL), 78–90, doi:10.1016/j.ijggc.2012.09.018.

Scholz, C. H. (2006), The strength of the San Andreas Fault: A critical analysis, in *Earthquakes: Radiated Energy and the Physics of Faulting*, *Geophys. Monogr.*, vol. 170, edited by R. Abercrombie et al., pp. 301–311, AGU, Washington, D. C.

Şengör, A. M. C., N. Görür, and F. Şaroğiu (1985), Strike-slip faulting and related basin formation in zones of tectonic escape: Turkey as a case study, in *Strike-Slip Deformation, Basin Formation, and Sedimentation*, *Soc. Sediment. Geol.*, pp. 227–264, SEPM, Tulsa, Okla.

Şengör, A. M. C., O. Tüysüz, C. İmren, M. Sakınç, H. Eyidoğan, N. Görür, X. Le Pichon, and C. Rangin (2005), The North Anatolian Fault: A new look, *Annu. Rev. Earth Planet. Sci.*, *33*(1), 37–112, doi:10.1146/annurev.earth.32.101802.120415.

Sibson, R. H. (1990), Faulting and fluid flow, in *Fluids in Tectonic Regimes of the Continental Crust: Short Courses Handbook*, edited by B. E. Nesbitt, pp. 93–132, Mineralogical Association of Canada, Québec City, Canada.

Sone, H., T. Shimamoto, and D. E. Moore (2012), Frictional properties of saponite-rich gouge from a serpentinite-bearing fault zone along the Gokasho-Arashima Tectonic Line, central Japan, *J. Struct. Geol.*, *38*, 172–182, doi:10.1016/j.jsg.2011.09.007.

Stein, R. S., A. Barka, and J. H. Dieterich (1997), Progressive failure on the North Anatolian fault since 1939 by earthquake stress triggering, *Geophys. J. Int.*, *128*, 594–604, doi:10.1111/j.1365-246X.1997.tb05321.x.

Stewart, M. A., R. E. Holdsworth, and R. A. Strachan (2000), Deformation processes and weakening mechanisms within the frictional-viscous transition zone of major crustal faults: Insights from the Great Glen Fault zone, Scotland, *J. Struct. Geol.*, *22*, 543–560.

Straub, C., H.-G. Kahle, and C. Schindler (1997), GPS and geologic estimates of the tectonic activity in the Marmara Sea region, NW Anatolia, *J. Geophys. Res.*, *102*(B12), 27,587–27,601, doi:10.1029/97JB02563.

Tanaka, H., K. Fujimoto, T. Ohtani, and H. Ito (2001), Structural and chemical characterization of shear zones in the freshly activated Nojima fault, Awaji Island, southwest Japan, *J. Geophys. Res.*, *106*(B5), 8789–8810, doi:10.1029/2000JB900444.

Temiz, U., Y. E. Gökten, and J. Eikenberg (2013), Strike-slip deformation and U/Th dating of travertine deposition: Examples from North Anatolian Fault Zone, Bolu and Yeniçağ Basins, Turkey, *Quat. Int.*, *312*, 132–140, doi:10.1016/j.quaint.2013.08.034.

Tenthorey, E., C. H. Scholz, E. Aharonov, and A. Léger (1998), Precipitation sealing and diagenesis: 1. Experimental results, *J. Geophys. Res.*, *103*(B10), 23,951–23,967, doi:10.1029/98JB02229.

Thomas, M. Y., J.-P. Avouac, J.-P. Gratier, and J.-C. Lee (2014a), Lithological control on the deformation mechanism and the mode of fault slip on the Longitudinal Valley Fault, Taiwan, *Tectonophysics*, *632*, 48–63.

Thomas, M. Y., J.-P. Avouac, J. Champenois, J.-C. Lee, and L. C. Kuo (2014b), Spatiotemporal evolution of seismic and aseismic slip on the Longitudinal Valley Fault, Taiwan, *J. Geophys. Res. Solid Earth*, *119*, 5114–5139, doi:10.1002/2013JB010603.

Titus, S. J., C. DeMets, and B. Tikoff (2006), Thirty-five-year creep rates for the creeping segment of the San Andreas Fault and the effects of the 2004 Parkfield earthquake: Constraints from alignment arrays, continuous Global Positioning System, and creepmeters, *Bull. Seismol. Soc. Am.*, *96*(4B), 250–268, doi:10.1785/0120050811.

van Noort, R., H. J. M. Visser, and C. J. Spiers (2008), Influence of grain boundary structure on dissolution controlled pressure solution and retarding effects of grain boundary healing, *J. Geophys. Res.*, *113*, B03201, doi:10.1029/2007JB005223.

Verbene, B. A., O. Plumper, D. A. Matthijs de Winter, and C. J. Spiers (2014), Superplastic nanofibrous slip zones control seismogenic fault friction, *Science*, *346*(6213), 1342–1344.

Wheeler, J. (2014), Dramatic effects of stress on metamorphic reactions, *Geology*, *42*(8), 647–650, doi:10.1130/G35718.1.

Wibberley, C. A. J., and T. Shimamoto (2003), Internal structure and permeability of major strike-slip fault zones: The Median Tectonic Line in Mie Prefecture, Southwest Japan, *J. Struct. Geol.*, *25*, 59–78.

Wilson, M., A. Tankut, and N. Guleç (1997), Tertiary volcanism of the Galatia province, north-west Central Anatolia, Turkey, *Lithos*, *42*(1–2), 105–121, doi:10.1016/S0024-4937(97)00039-X.

Wilson, M. J. (2004), Weathering of the primary rock-forming minerals: Processes, products and rates, *Clay Miner.*, *39*(3), 233–266, doi:10.1180/0009855043930133.

Yildirim, C., T. F. Schildgen, H. Echtler, D. Melnick, and M. R. Strecker (2011), Late Neogene and active orogenic uplift in the Central Pontides associated with the North Anatolian Fault: Implication for the northern margin of the Central Anatolian Plateau, Turquey, *Tectonics*, *30*, TC5005, doi:10.1029/2010TC002756.

Zubtsov, S., F. Renard, J.-P. Gratier, R. Guiguet, D. K. Dysthe, and V. Traskine (2004), Experimental pressure solution compaction of synthetic halite/calcite aggregates, *Tectonophysics*, *385*(1–4), 45–57, doi:10.1016/j.tecto.2004.04.016.